



# Simulation of a wall-mounted stem in uniform flow

Weilin Chen<sup>1</sup>  and Yuzhu Pearl Li<sup>1</sup> 

<sup>1</sup>Department of Civil and Environmental Engineering, National University of Singapore, Singapore 117576, Republic of Singapore

**Corresponding authors:** Weilin Chen, [wl.chen@nus.edu.sg](mailto:wl.chen@nus.edu.sg); Yuzhu Pearl Li, [pearl.li@nus.edu.sg](mailto:pearl.li@nus.edu.sg)

(Received 23 July 2024; revised 13 March 2025; accepted 18 April 2025)

The dynamics of wall-mounted flexible structures, such as aquatic vegetation, is essential for analysing collective behaviours, flow distributions and vortex formation across different scales. To accurately model these structures under various flow conditions, we develop a novel numerical method that couples the immersed boundary method (IBM) with the vector form intrinsic finite element (VFIFE) method, referred to as the IBM–VFIFE method. We simulate both flexible and rigid stems, each with a constant aspect ratio of 10, mounted on an impermeable bottom in uniform flow with the Reynolds number ranging from 200 to 1000. In the rigid case, we identify three distinct flow regimes based on the vortex dynamics and lift spectral characteristics. Due to the influences of downwash flow at the free end and upwash flow near the junction, vortex shedding varies significantly along the vertical direction. For the flexible case, we examine a wide range of stem stiffness values to explore potential dynamic responses. The results reveal that stiffness plays a key role in stem behaviour, leading to three distinct classifications based on amplitude magnitude and displacement spectra respectively. Notably, the vortex dynamics of a flexible stem differs significantly from that of a rigid stem due to shape deformation and stem oscillation. A flexible stem with relatively high stiffness experiences greater hydrodynamic loads compared with its rigid counterpart. This study highlights the unique stem behaviours and vortex dynamics associated with flexible stems. We find that stem oscillation, combined with a near-wake base vortex, contributes to an upwash flow near the stem bottom, which significantly weakens (or, in some cases, eliminates) the downwash flow. Additionally, low-frequency oscillations in the streamwise and vertical directions are observed, while the transverse oscillation exhibits a dominant frequency one order of magnitude higher. Overall, this study provides valuable insights into the response and vortex dynamics of a single stem in uniform flow.

**Key words:** flow-structure interactions, vortex dynamics, vortex interactions

## 1. Introduction

Flow over the finite wall-mounted cylinder (FWMC) exhibits complex flow structures and vortex–vortex interactions due to geometric modifications at the free end and the cylinder–wall junction (Finnigan 2000; Krajnovic 2011; Nepf 2012). This phenomenon is widely observed in engineering applications, such as high-rise buildings and aquatic vegetation. Understanding the emergence, development and interaction of vortical structures with different rotations is crucial for advancing the fundamental theory of FWMC flow (Wang & Zhou 2009; Zhu *et al.* 2017; Yauwenas *et al.* 2019; Cao *et al.* 2022). Over the past few decades, significant progress has been made in uncovering the underlying physics of FWMC flow (Adaramola *et al.* 2006; Wang & Zhou 2009; Luhar & Nepf 2011; Li & Fuhrman 2022; Hu & Li 2023; Hu, Huang & Li 2023). A comprehensive review of these findings is essential to establish a foundational understanding before addressing more multifaceted configurations, such as fluid–structure interaction (FSI) of wall-mounted flexible structures with varying flexibility (or stiffness).

### 1.1. Flow over the finite wall-mounted rigid structure

Based on cross-sectional shape, structures can be classified into three categories (Derakhshandeh & Alam 2019). The first structure consists of a continuous and finite curvature shape, such as a circular or elliptical cylinder (e.g. most of the stems), while the second one is sharp edged with an infinitely large curvature, for example, a square or triangular cylinder (e.g. plates or walls). The third one is a hybrid of the two, and a typical case is a semi-circular cylinder (e.g. breakwater structures). Studies of FWMC have primarily focused on the first two categories, as they are more prevalent in natural and engineered environments. We start with these two types of wall-mounted structures, providing a detailed discussion of the flow structures of a rigid FWMC. Differences arising from cross-sectional shape are highlighted when relevant.

Flow structures around a circular FWMC are strongly influenced by the aspect ratio ( $AR = l/D$ , where  $l$  is the height of the structure and  $D$  is the diameter or side length), Reynolds number ( $Re = U_\infty D/\nu$ , where  $U_\infty$  is incoming flow velocity and  $\nu$  is the fluid kinematic viscosity), boundary layer thickness ( $\delta/D$ ), and turbulent intensity ( $T_i = u'/U_\infty$ , where  $u'$  is the root-mean-square (r.m.s.) of the turbulent velocity fluctuation), among other factors (Sakamoto & Arie 1983; Bourgeois, Sattari & Martinuzzi 2011; Porteous, Moreau & Doolan 2014; Hearst, Gomit & Ganapathisubramani 2016). Based on the time-averaged distribution of vortical structures, the wake of an FWMC can be divided into three types (Zhang *et al.* 2017), i.e. dipole type (i.e. one pair of the streamwise vortices at the upper part), quadrupole type (i.e. two pairs of the streamwise vortices at the upper and lower parts) and six-vortex type (i.e. transitional structures involved). Particular vortical structures of the FWMC with a height over the critical value are presented in figure 1. The transition from dipole to quadrupole is marked by a critical aspect ratio (Sumner, Heseltine & Dansereau 2004; Wang & Zhou 2009; Hosseini, Bourgeois & Martinuzzi 2013; Sumner 2013). When the height exceeds this critical value, a tip vortex pair and a base vortex pair appear at the free end and junction, respectively (Bourgeois *et al.* 2011; Hajimirzaie, Wojcik & Buchholz 2012; Porteous *et al.* 2014). The appearance of these vortex pairs is highly dependent on the AR. A sufficiently thick boundary layer and AR above the critical value promote the formation of the tip vortex pair at the free end (Sumner *et al.* 2004; Adaramola *et al.* 2006; Sumner & Heseltine 2008; Bourgeois *et al.* 2011, 2012; Sumner 2013). The origin of the tip vortex differs depending on the cross-sectional shape. In a square FWMC, streamwise vorticity near the free end arises from the reorientation of vertical vorticity in the sidewall shear layers

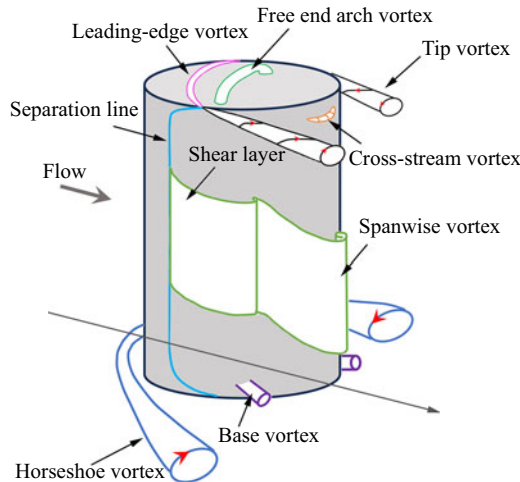


Figure 1. The sketch of the vortical structures for flow over a wall-mounted rigid circular cylinder. The sketch is based on the models proposed by Pattenden *et al.* (2005), Frederich *et al.* (2007), Krajnovic (2011), Zhu *et al.* (2017) and Essel, Tachie & Balachandar (2021). Note that only part of the shear layer and spanwise vortex are shown.

due to lateral vorticity of the free-end shear layer (Bourgeois *et al.* 2011). Here, the tip vortex is essentially a deformed Kármán vortex. In contrast, for a circular FWMC, the tip vortex originates from the leading or trailing edge of the free end and is not associated with the Kármán vortex (Hunt *et al.* 1978; Kawamura *et al.* 1984; Hwang & Yang 2004; Pattenden, Turnock & Zhang 2005; Hain, Kahler & Michaelis 2008; Palau-Salvador *et al.* 2010; Krajnovic 2011; Saeedi, LePoudre & Wang 2014). This highlights the pivotal role of cross-sectional shape in the tip vortex generation.

When  $AR > 3$ , the base vortex pair forms at the junction (Sumner *et al.* 2004; Adaramola *et al.* 2006), developing behind the cylinder and inducing an upwash flow (Etzold & Fiedler 1976; Hajimirzaie *et al.* 2012). Its formation is strongly influenced by  $\delta/D$  (Wang *et al.* 2006). Compared with the tip vortex pair, the base vortex pair is weaker and dissipates more quickly downstream.

The trailing vortex (not shown in figure 1), which is typically located far from the free end, is not a continuation of the tip vortex pair. According to Frederich, Wassen & Thiele (2008) and Palau-Salvador *et al.* (2010), it arises from strong downwash effects and associated upwash motion away from the wake centreline, triggered by the finite cylinder width. Initially believed to be visible only in the mean flow field (Fröhlich & Rodi 2004), tomographic particle image velocimetry results from Zhu *et al.* (2017) suggest that this structure can also be observed in the instantaneous flow field where  $AR$  is low.

Vortex shedding from FWMC sidewalls is influenced by the  $AR$  and boundary layer conditions, primarily due to variations in downwash flow and near-wake base vortices (Fröhlich and Rodi, 2004; Pattenden *et al.* 2005; Wang *et al.* 2006; Palau-Salvador *et al.* 2010; Tsutsui 2012). A thick boundary layer could enhance the base vortex and induce upwash flow. Spanwise vortices can adopt antisymmetric and/or symmetric patterns depending on upwash and downwash flow (Wang *et al.* 2006; Wang & Zhou 2009). For FWMC with larger  $AR$ , both types of vortex shedding may coexist. Wang, Cao & Zhou (2014) found that vortex shedding near the free end is predominantly symmetric, whereas alternating vortex shedding dominates the wake near the centre and lower regions. The separation line (shown in figure 1), corresponding to points where the shear layers detach

from the side surface, indicates that separation occurs earlier around the centre than near the free end or lower part due to the influences of downwash and upwash flow.

The free-end arch vortex appears in the mean wake field when  $AR < 3$  (Lee 1997; Krajnovic 2011). This vortex takes on a reversed U-shape (Fröhlich and Rodi, 2004). The legs of the mean arch vortex are inclined in the streamwise direction at a relatively constant angle (Krajnovic 2011). For low  $AR$  cases, the dominant downwash effect increases the likelihood of symmetric vortex shedding (Wang *et al.* 2014). This symmetric shedding may induce instantaneous arch vortex formation in short cylinders (Zhu *et al.* 2017).

In front of the arch vortex, the leading-edge vortex forms at the forward half of the free end surface (Kawamura *et al.* 1984; Krajnovic 2011). This vortex is attributed to the reverse flow along the centre of the free end surface, which is entrained by the separated flow from the leading edge (Kawamura *et al.* 1984; Pattenden *et al.* 2005; Palau-Salvador *et al.* 2010; Krajnovic 2011). The attachment length of this vortex is strongly affected by both  $AR$  and  $Re$  (Sumner 2013). Downstream of the surface, the forward free-end flow interacts with the wake behind the FWMC, leading to the emergence of the upper near-wake cross-stream vortex (as shown in figure 1). Additional vortices may also form, such as the horseshoe vortex at the junction. The horseshoe vortex may interact with the vortices behind the FWMC, significantly influencing the overall wake dynamics.

The flow structures around the FWMC are highly complex, with their formation, development and dissipation closely tied to the vortex interactions, including rotational effects, upwash and downwash flows. The FWMC height and boundary layer conditions play crucial roles in this dynamics. In this study, we focus on the hydrodynamic forces and vortex dynamics of a circular FWMC across a wide range of  $Re$ . Specific flow behaviours are analysed, and distinctive vortex structures are reported.

## 1.2. Flow over the finite wall-mounted flexible structure

When the structure is flexible, FSI becomes significant. In nature, wall-mounted structures appear in various forms, such as flexible plate, blade, filament, aquatic plant and stem. Research on these structures is essential for understanding their behaviours under different flow conditions. However, most studies have focused on predicting drag, wave attenuation, flow profiles and structural reconfiguration, with relatively few investigations into their vortex dynamics. Furthermore, the parameters considered in these studies are scattered, making it difficult to establish a comprehensive understanding of FSI of wall-mounted flexible structures.

Zeller *et al.* (2014) proposed a novel formulation of the Keulegan–Carpenter number ( $KC = U_m T/D$ , where  $U_m$  is the maximum flow velocity and  $T$  is the oscillatory period) for predicting drag coefficients and developed a model for wave attenuation. They estimated the averaged turbulence production over the wave period using the maximum flow velocity and the relative velocity between the current and waves. Mullarney *et al.* (2010) demonstrated that stem stiffness significantly affects its motion relative to the wave under wave forcing. A highly flexible stem moves with the surrounding water, whereas a stiff stem exhibits minimal motion, leading the surrounding water by  $90^\circ$ . They developed an analytical model to describe the wave-forced motion of a single stem and derived an equation to predict frequency-dependent wave dissipation. Luhar & Nepf (2016) observed that blade motion is governed mainly by two dimensionless parameters: (i) the Cauchy number ( $Ca$ ) and (ii) the ratio of the blade length to wave orbital excursion. Here,  $Ca$  is defined as  $Ca = 0.5\rho_f D l^3 U_{ref}^2 / EI$ , where  $\rho_f$  is the fluid density,  $D$  is the side length or stem diameter,  $l$  is the stem height,  $E$  is Young's modulus,  $I$  is the cross-sectional momentum of inertia and  $U_{ref}$  is the incoming flow velocity. When  $Ca \gg 1$ , drag on

the flexible blade is lower. However, when  $Ca \sim O(1)$ , drag is higher than that of a rigid blade. Hu *et al.* (2021) developed a theoretical model to predict the motion of rigid and flexible stems under wave conditions, identifying a phase lag between flow motion and stem response. Zhang & Nepf (2022) developed a scaling equation to predict the reconfiguration of flexible plants with leaves due to the hydrodynamic drag using water channel experiments and numerical simulations.

In terms of flexible filaments, Silva-Leon & Cioncolini (2020) experimentally investigated their motions and identified different filament responses, including static reconfiguration, small-amplitude vibration, large-amplitude periodic vibration and large-amplitude aperiodic vibration. These behaviours were found to be influenced by  $Re$  and the filament length ( $l$ ). Huang, Shin & Sung (2007) numerically observed bistability in flexible filaments by varying their length. Revstedt (2013) studied the deformation of a flexible cantilever at  $Re = 400$  and a reduced velocity range of  $\pi/4 - 2\pi$ . In the desynchronisation regime, the stem motion has negligible effects on vortical structures, whereas in the synchronisation regime, the stem significantly alters the mean flow field, frequencies and vortical structures. Zhang, He & Zhang (2020) explored the dynamics of a wall-mounted flexible filament by varying the bending rigidity, mass ratio ( $m^* = m/m_f$ , where  $m$  is the structure mass and  $m_f$  is the displaced fluid mass) and  $Re$ . They observed three distinct dynamic modes, referred to as lodging, regular vortex-induced vibration (VIV) and static reconfiguration. In regular VIV, the filament frequency locks onto the second natural frequency. However, when the filament is with a nearly upright orientation, the vortex shedding is weak and no lock-in is observed. At higher  $Re$ , vortex shedding intensifies, leading to first-mode frequency lock-in, as reported in Py, De Langre & Moulia (2006) and Jin *et al.* (2018). Rota *et al.* (2024) observed two flapping states of a wall-mounted flexible filament in turbulent wall flow by direct numerical simulations. One state is with a more flexible filament which oscillates at the frequency of the largest eddies, and the other is with a more rigid filament which is governed by the structural natural frequency.

For a single stem, Jacobsen *et al.* (2019) experimentally studied its motion subjected to regular waves, focusing on several critical aspects: (i) predicting the stem motion and static shape, (ii) force reduction due to flexibility, (iii) hydrodynamic forces on the flexible stem, (iv) estimating external hydrodynamic loading and internal shear forces and (v) examining the relationship between phase lags and internal shear forces. They found that when the stem is stiffer, the phase lags remain nearly uniform along its length, whereas in more flexible stem, phase lags vary. The drag force shows better overall coherence with varying  $KC$ . Toward the stem base, shear force increases monotonically for certain stems; however, it reaches local maximum near the stem tip. Zhu *et al.* (2020) developed a consistent-mass cable model to solve the flow and flexible stem interaction. They observed that, even under symmetric waves, the blade can experience asymmetric motion, with asymmetry of the tip motion growing with wave height and blade length but reducing as flexural rigidity increases. Using numerical simulations, O'Connor & Revell (2019) investigated the dynamic behaviours of a two-dimensional (2-D) flexible flap in channel flow. They identified four different response modes: static, flapping, period doubling and chaotic motion. Additionally, they discussed the stabilising and destabilising effects of the bending stiffness and mass ratio. Leclercq & de Langre (2018) observed four kinematic regimes, referred to as the fully static, large-amplitude, convective and modal regimes, based on the flow oscillation amplitude and frequency relative to the blade dimensions and natural frequency. Jin *et al.* (2019) experimentally examined the unsteady dynamics of individual wall-mounted flexible plates with varying rigidities. They identified three dominant modes



of tip oscillation: flutter, twisting and orbital modes. Neshamar *et al.* (2022) experimentally investigated the flow-induced oscillation of a cantilevered cylinder. They found that, depending on the reduced velocity, the dominant response could manifest as in-line vibration, figure-eight vibration or transverse vibration, each with distinct features. They further developed an empirical model to reasonably predict the amplitude of in-line vibration.

Although significant progress has been made in recent years, several key questions remain unsolved, which are critical for both engineering applications and theoretical advancements. (i) Amongst existing studies, the three-dimensional (3-D) vortical structures, particularly their spatial evolution, remain largely unexplored, despite their central role in flow physics. (ii) The complex dynamics of a flexible stem is closely associated with unsteady vortex shedding events (Lunar and Nepf, 2016), and these interactions play a crucial role in regulating the system's behaviour. (iii) Most theoretical and experimental studies have overlooked motion-induced forces, despite their demonstrated significance in force amplification (Triantafyllou *et al.* 2016). Among the different motion components, transverse motion makes the greatest contribution to force amplification, exceeding the streamwise and vertical motion effects. (iv) The tip motion and dynamic distributions along the vertical direction need to be clarified.

### 1.3. The objective of the present study

In this study, we introduce, for the first time, a coupled immersed boundary method (IBM)–vector form intrinsic finite element (VFIFE) method to simulate wall-mounted structures. This novel approach enables us to address several unexplored aspects of uniform flow over a circular FWMC. We start with a wall-mounted rigid stem to provide a foundational understanding of the vortex dynamics and to facilitate comparisons with flexible stems. We then shift our focus to the FSI of a wall-mounted flexible stem. The remains of this study are structured as follows. In § 2, we provide the details of the numerical methodology adopted in this study. In § 3, we validate the developed model through a comparison with theoretical and experimental results. In § 4, we present the details of the parameters applied in the simulation of the wall-mounted stem. In § 5, we present the flow over the rigid stem and discuss the evolution of the 3-D vortical structures. Additionally, we analyse the development of upwash and downwash flows and inherent 3-D wake instabilities. In § 6, the FSI response and vortex dynamics of a flexible stem are presented. In § 7, we further discuss several phenomena in the flexible case. In § 8, the main findings of this study are summarised.

## 2. Methodology

In this section, we present the adopted numerical method for simulating the wall-mounted structure. In § 2.1, the filtered Navier–Stokes (N-S) and continuity equations in the large-eddy simulation are presented. In §§ 2.2 and 2.3, the details of VFIFE and IBM are introduced. In § 2.4, information on the coupling between the fluid and structure is provided.

### 2.1. Large-eddy simulation (LES)

The governing equations for the incompressible flow are the filtered N-S and continuity equations expressed as follows:

$$\left. \begin{aligned} \frac{\partial \bar{u}_i}{\partial t} + \bar{u}_j \frac{\partial \bar{u}_i}{\partial x_j} &= -\frac{1}{\rho_f} \frac{\partial \bar{p}}{\partial x_i} + \nu \frac{\partial^2 \bar{u}_i}{\partial x_j \partial x_j} - \frac{\partial \tau_{ij}}{\partial x_j} + f_i \\ \frac{\partial \bar{u}_i}{\partial x_i} &= 0. \end{aligned} \right\} \quad (2.1)$$

Here,  $u_i$  ( $i = 1, 2, 3$ ) is the flow velocity of three directions in the Cartesian coordinate system, an overbar stands for the filtering procedure,  $p$  is the pressure,  $t$  is the time,  $\rho_f$  is the fluid density,  $\nu$  is the kinematic viscosity of the fluid,  $f_i$  is the extra force that represents the action of immersed objects on the fluid and  $\tau_{ij}$  is the subgrid-scale stress, representing the influences of the filtered small-scale turbulent structures on the flow field (Smagorinsky 1963). To ensure the closure of (2.1), the Smagorinsky eddy viscosity model is applied, which is given as

$$\tau_{ij} = 2 (C_s \Delta)^2 |\bar{S}| \bar{S}_{ij} + \frac{1}{3} \tau_{kk} \delta_{ij}, \quad (2.2)$$

where  $C_s$  is the Smagorinsky constant. In the present study,  $C_s = 0.1$  (Deardorff 1970). The filter width  $\Delta$  is adopted as  $\Delta = \sqrt[3]{\Delta x \Delta y \Delta z}$  with  $\Delta x$ ,  $\Delta y$ , and  $\Delta z$  as the grid sizes in the three directions. Here,  $|\bar{S}| = (2\bar{S}_{ij}\bar{S}_{ij})^{1/2}$  is the magnitude of large-scale strain rate tensor, where  $\bar{S}_{ij} = (1/2)((\partial \bar{u}_i / \partial x_j) + (\partial \bar{u}_j / \partial x_i))$ .

## 2.2. Vector form intrinsic finite element

The VFIFE method was first introduced by Ting, Shih & Wang (2004a,b, 2012), Ting & Wang (2008) and Shih, Wang & Ting (2004). It is an analytical and numerical method in structural mechanics based on point value description and vector form theory. The point value description in the VFIFE method relies on a lumped mass matrix, meaning that external force on one spatial point does not influence the motion dynamics of other spatial points. As a result, the method eliminates the need to construct complex rigidity matrix or solve large-scale nonlinear equations. Compared with conventional methods, the VFIFE method effectively avoids certain nonlinear issue that arise when structures undergo large deformations, dislocations, collisions or elastoplastic behaviours, such as iteration non-convergence and matrix singularity. Additionally, by appropriately discretising path elements, the characteristics between two path elements can be adjusted, allowing the method to handle structural discontinuities. Consequently, the VFIFE method has been widely applied to address challenging nonlinear and discontinuous scenarios (Duan *et al.* 2014; Xu *et al.* 2015; Xu & Lin 2017; Hou, Fang & Zhang 2018; Li, Wei & Bai 2020; Wu *et al.* 2020).

The foundation of the VFIFE lies in its spatial and temporal structural point value description. In the spatial point value description, the structural mass is concentrated at a series of discretised spatial points. The motion and deformation of structure can be determined through the positions of these spatial points, which are interconnected by linear beam elements, see figure 2(a). It is assumed that the cross-sectional profiles of the elements remain identical and perpendicular to the principal axis at any position. Unlike conventional methods, the beam elements in the VFIFE are responsible solely for internal structural force and are independent of the governing equations. For cases involving multiple internal forces between two spatial points, multiple beam elements are used. These elements are positioned between the two spatial points to represent the internal force without needing to define it across the entire structural range (Ting, Duan & Wu 2012).

In the temporal point value description, the structure's dynamics is represented by a series of path elements that follow the principle of 'large dislocation and small deformation'. Within each path element, the shift of a spatial point comes from the two components: rigid body motion and pure deformation. The displacement due to rigid body motion is determined using Newton's second law and the rotational equation, while the displacement caused by pure deformation is described by Hooke's law through the introduction of a virtual reverse motion. Ensuring consistency of the structural properties and motion trajectories is crucial for accurately calculating pure deformation within each path unit via reverse motion. In the VFIFE, reverse motion is introduced to distinguish

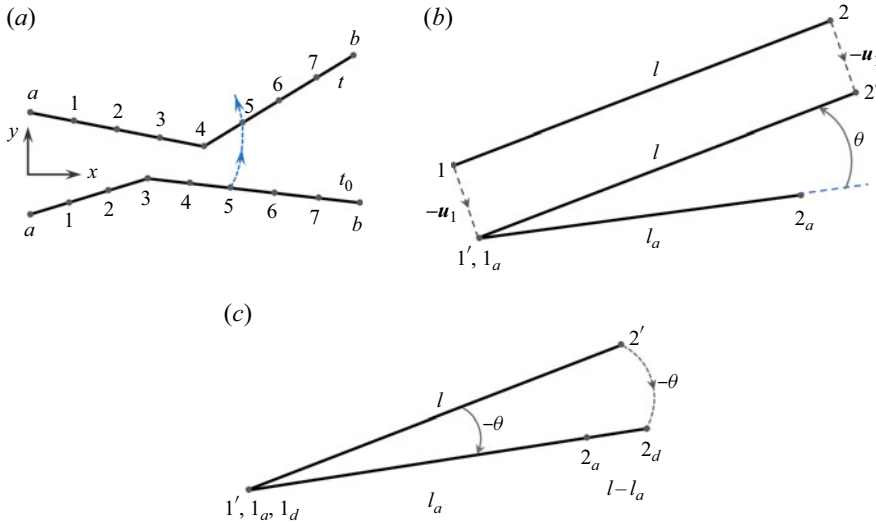


Figure 2. (a) The beam elements, (b) reverse translation and (c) reverse rotation in the VFIFE.

dislocations caused by rigid body movement from those caused by pure structural deformation, see [figure 2\(b,c\)](#). The processing steps are as follows. (i) The calculation of structural internal force is based on the state at the initial instant  $t_a$ . (ii) Due to the consistency of structural properties and motion trajectories within each path element, a virtual structural state at any instant  $t$  is generated through a virtual reverse motion, which includes reverse translational and rotational motions for the spatial position at that instant. Subsequently, minor dislocations and deformations are identified by comparing the reference and virtual structural states. (iii) These small deformations and dislocations are then resolved using the structural deformation–internal force relationship. Finally, the structural state at  $t_b$  is obtained through a forward rigid body motion.

The dynamics of a wall-mounted flexible stem is simulated using VFIFE method. Based on the point value description, the stem is discretised into a set of spatial nodes that connect to each other by beam elements. The motion of each node is applied to describe the movement and deformation of the stem and satisfies Newton's second law

$$\left. \begin{aligned} m\dot{\mathbf{V}} + \zeta m\mathbf{V} + \mathbf{F}^{int} &= \mathbf{F}^{ext} \\ I\dot{\boldsymbol{\omega}} + \zeta I\boldsymbol{\omega} + \mathbf{M}^{int} &= \mathbf{M}^{ext} \end{aligned} \right\}, \quad (2.3)$$

where  $m$  and  $I$  are the mass and momentum of inertia matrix of the node, respectively. Here,  $\dot{\mathbf{V}}$ ,  $\mathbf{V}$ ,  $\dot{\boldsymbol{\omega}}$  and  $\boldsymbol{\omega}$  are the acceleration, velocity, angular acceleration and angular velocity of the node, respectively,  $\mathbf{F}^{int}$ ,  $\mathbf{F}^{ext}$ ,  $\mathbf{M}^{int}$  and  $\mathbf{M}^{ext}$  are the internal force, external force, internal momentum and external momentum, respectively, and  $\zeta$  is the structural damping coefficient, which is zero in the present study. An explicit iterative scheme based on the central difference is adopted to solve equation (2.3) as follows:

$$\left. \begin{aligned} \mathbf{x}^{n+1} &= \Delta t_s^2 \frac{\mathbf{F}^{ext} - \mathbf{F}^{int}}{m} + 2\mathbf{x}^n - \mathbf{x}^{n-1} \\ \boldsymbol{\alpha}^{n+1} &= \Delta t_s^2 \frac{\mathbf{M}^{ext} - \mathbf{M}^{int}}{I} + 2\boldsymbol{\alpha}^n - \boldsymbol{\alpha}^{n-1} \\ \mathbf{V}^{n+1} &= \frac{\mathbf{x}^{n+1} - \mathbf{x}^n}{\Delta t_s}, \quad \boldsymbol{\omega}^{n+1} = \frac{\boldsymbol{\alpha}^{n+1} - \boldsymbol{\alpha}^n}{\Delta t_s} \end{aligned} \right\}, \quad (2.4)$$

where  $\mathbf{x}$ ,  $\boldsymbol{\alpha}$  and  $\Delta t_s$  represent the node position, rotation angle of the node and the structural time step, respectively. The temporal trajectory of any node on the stem is described by a set of spatial points, and the process between the spatial points is defined as



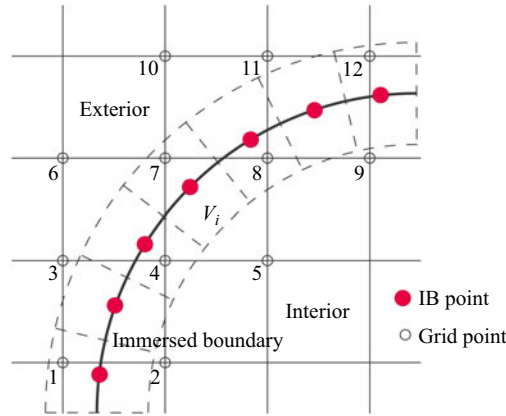


Figure 3. The layout of the immersed boundary method. The discrete volumes ( $V_i$ ) of the immersed boundary points (IBPs), marked by the dashed region, form a thin shell of thickness equal to one mesh width around each IBP.

the path element. Proper division of the path element allows the properties of each node to vary between two elements.

### 2.3. Immersed boundary method

The IBM was first introduced by Peskin (1972) for simulating blood flow around the flexible leaflet of a human heart. Compared with conventional numerical methods, IBM offers key advantages, particularly in FSI simulations involving topological changes. Another significant advantage is its parameterised and fast implementation, enabling the rapid simulation of numerous cases with different geometric configurations, unlike conventional methods that rely on body-conformal grids. In the IBM framework, the flow motion equations are discretised on a fixed Cartesian grid, while the structure is represented by a series of IBPs on a Lagrangian grid, which is curvilinear and free to move, see figure 3. The Cartesian grid does not conform to the geometry of a moving structure. As a result, the boundary conditions on the fluid–body interface cannot be imposed directly. Instead, an extra body force is incorporated into the fluid momentum equation to account for this interaction. This body force is updated during pressure iterations (Ji, Munjiza & Williams 2012), ensuring that it is solved simultaneously with pressure and that the boundary condition on the immersed boundary is fully satisfied. In the current simulation, the stem is discretised into 160 elements along its height, resulting in 161 circular slices. Each slice is represented as a circle, further discretised into 256 IBPs uniformly distributed along its circumferences, as illustrated in figure 4(c). This ensures that at least one IBP is present in each grid cell, maintaining accurate spatial resolution. Given an aspect ratio of  $AR = 10$ , the resolution is  $1/16$ . Notably, when the stem deforms, the plane of each layer, composed of 256 IBPs, remains perpendicular to the tangent line at the corresponding node. As the structure’s surface is formed by these IBPs, the internal fluid remains entirely isolated from the external fluid, inherently satisfying the condition of a zero normal pressure gradient on the surface.

To discretise equation (2.1), the second-order Adams–Bashforth time scheme and the second-order central difference scheme are applied, which lead to the following conservation form:

$$\left. \begin{aligned} \mathbf{u}^{n+1} &= \mathbf{u}^n + \delta t \left( \frac{3}{2} \mathbf{h}^n - \frac{1}{2} \mathbf{h}^{n-1} - \frac{3}{2} \nabla p^n + \frac{1}{2} \nabla p^{n-1} \right) + \mathbf{f}^{n+\frac{1}{2}} \delta t \\ \nabla \cdot \mathbf{u}^{n+1} &= 0, \end{aligned} \right\} \quad (2.5)$$

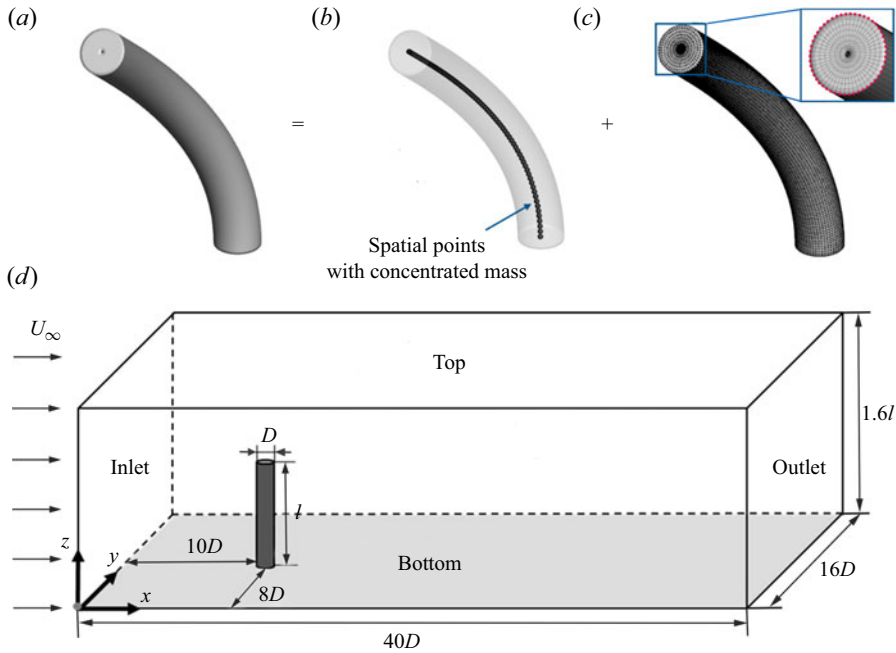


Figure 4. (a,b,c) The wall-mounted flexible stem model in the present simulation and (d) the numerical set-up of the computational domain (not to scale). Part of the IBPs on the top surface are marked by the red dots in (c).

where  $\mathbf{h} = \nabla \cdot (-\mathbf{u}\mathbf{u} + (v + v_t)(\nabla\mathbf{u} + \nabla\mathbf{u}^T))$  is composed of the convective and diffusive terms, in which the superscript  $T$  is the transpose of a matrix and  $v_t$  is the turbulence eddy viscosity. Superscripts  $n+1$ ,  $n+1/2$ ,  $n$  and  $n-1$  indicate the time steps. The extra force  $\mathbf{f}$  is determined by setting the velocity consistent condition  $\mathbf{U}^{n+1} = \mathbf{V}^{n+1}$  on the fluid–structure interface, where  $\mathbf{U}^{n+1}$  is the interpolated fluid velocity and  $\mathbf{V}^{n+1}$  is the update structure velocity. Extra force  $\mathbf{f}$  is formally evaluated at the time step  $n + 1/2$

$$\mathbf{f}^{n+\frac{1}{2}}\delta t = D(\mathbf{F}^{n+\frac{1}{2}}) = D\left(\mathbf{v}^{n+1} - I\left(\mathbf{u}^n + \delta t\left(\frac{3}{2}\mathbf{h}^n - \frac{1}{2}\mathbf{h}^{n-1} - \frac{3}{2}\nabla p^n + \frac{1}{2}\nabla p^{n-1}\right)\right)\right), \quad (2.6)$$

where  $\mathbf{F}$  is the extra body force on the structure and  $\mathbf{v}^{n+1} = \mathbf{V}^{n+1} + \mathbf{r} \times \boldsymbol{\omega}^{n+1}$  is the desired velocity on the IBPs obtained by solving equation (2.3), in which  $\mathbf{r}$  is a vector from a node to an IBP. The interpolation and distribution functions,  $I$  and  $D$ , suggested in Peskin (1972) are applied, which are responsible for data transfer between the non-conforming Eulerian and Lagrangian grids.

#### 2.4. Coupling between the fluid and structures

As mentioned earlier, in the present method, the wall-mounted flexible stem is materialised by the IBPs on the solid surface, see figure 4(a–c). However, as the stem’s motion is defined by spatial points with concentrated mass, an appropriate approach is needed to effectively transfer the fluid force from the surface IBPs to these spatial points. During each iteration of fluid–structure coupling, the solid surface surrounding these mass points is reconstructed using IBPs, see figure 4(c). The fluid force on these reconstructed solid surface IBPs is then applied to the corresponding mass points as external forces. Consequently, the motion of each node is determined using (2.3). Simultaneously, the flow

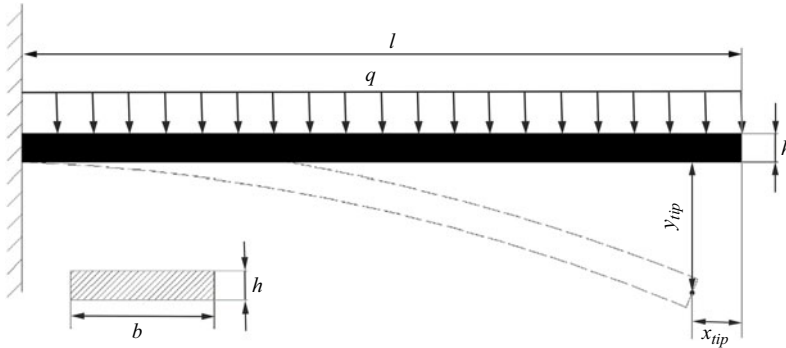


Figure 5. Model for the deformation of a flexible stem under uniform loading.

velocity and pressure are updated, and the velocity on the immersed boundary is corrected, thereby establishing the coupling between the fluid and the structure. It is important to note that the critical time step for solid motion is significantly smaller than that for the fluid. Therefore, within each fluid time step, the solid motion must be iterated multiple times under the assumption that the fluid forces remain unchanged.

### 3. Validation

#### 3.1. The deformation of a cantilever plate under uniform loading

First, we verify the codes for pure deformation of a wall-mounted flexible stem with a rectangular cross-section under uniform loading. As modelled in figure 5, the cantilever plate is wall mounted under uniform loading. The geometric parameters for the plate are the length ( $l$ ) of 5 cm, the width ( $b$ ) of 1 cm and the thickness ( $h$ ) of 0.2 cm. The plate density is  $0.678 \text{ g cm}^{-3}$ , the elastic modulus is  $5 \times 10^5 \text{ Pa}$  and Poisson's ratio is 0.4. The uniform loading varies in the range of  $q = 0.0001\text{--}0.0008 \text{ N cm}^{-1}$ . The plate is divided into elements, i.e. 10, 25 and 50. The corresponding grid in the vertical direction (along the length) is  $dx_s$ . For different situations, the time step is controlled to be smaller than the critical time step  $dt_s^0$  calculated using the equation of  $dt_s^0 = dx_s / \sqrt{E/\rho_s}$ , where  $E$  is Young's modulus, and  $\rho_s$  is the plate density. The structural damping is set as  $\zeta = 0$ .

Based on the deformation theory of a plate under uniform loading ( $q$ ), the final deformation curve follows the equation

$$v(x) = -\frac{qx^2}{24EI} (x^2 - 4xl + 6l^2), \quad (3.1)$$

where  $x$  is the distance of one point to the fixed end (positive in the  $x$  direction),  $v(x)$  is the final deformation of the plate and  $I = bh^3/12$  is the cross-sectional inertial moment of the plate.

Figure 6 shows the comparison of the simulated results and theoretical results. It is seen that the model for the plate motion can accurately predict the deformation of the plate. Further, the number of elements in the simulation is also essential. The difference (in percentage) between the simulation and the theoretical value becomes higher as it gets closer to the free end of the plate, which is related to the deformation growing smaller. Thus, it requires a higher number of elements. As shown in figure 7, after the element number exceeds 25, the simulated deformation and vibration frequency match very well the theoretical results. The relative difference generally gets smaller when the loading is higher. Here, the relative differences for the deformation and vibration frequency are

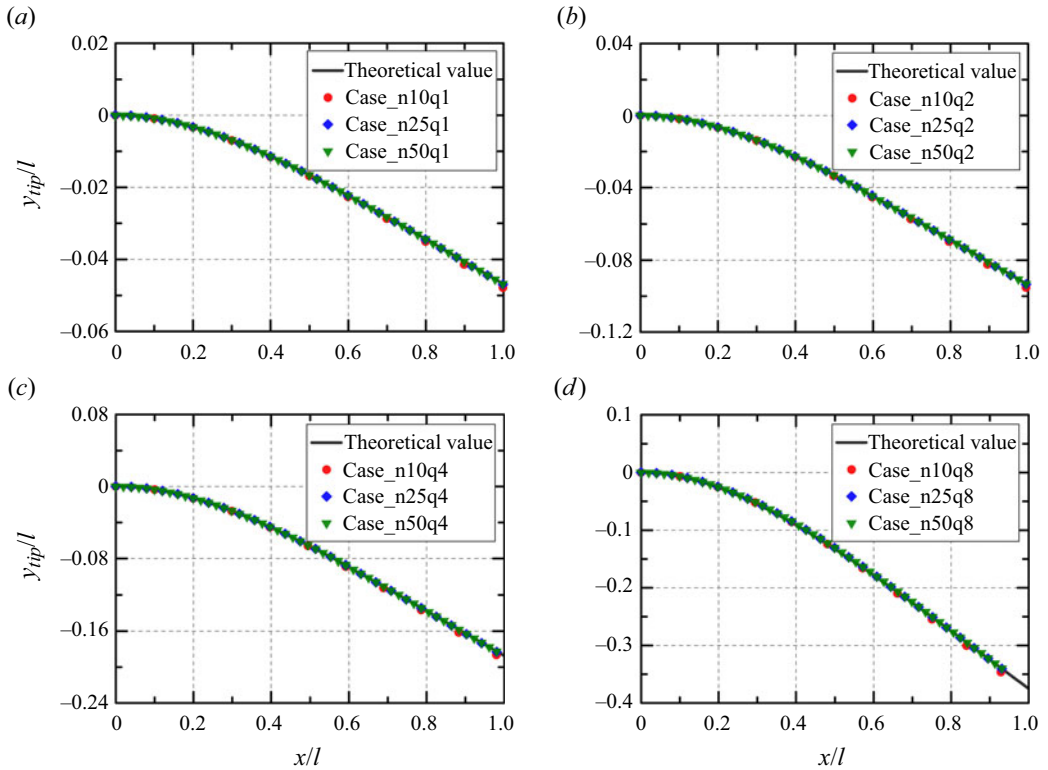


Figure 6. Comparison of the transverse shift of the tip with the theoretical value for a plate under uniform loading. Here, Case\_n10q1 represents the case of the plate divided into 10 elements and under the loading of  $q = 0.0001 \text{ N cm}^{-1}$ . The naming scheme is applied for other cases. For example, Case\_n25q8 denotes the case of the plate divided into 25 elements and under the loading of  $q = 0.0008 \text{ N cm}^{-1}$ .

defined as  $\Delta v_{tip} = (v_{tip} - v_{tip}^0)/v_{tip}^0$  and  $\Delta f_1 = (f_1 - f_1^0)/f_1^0$ , respectively, where  $v_{tip}$  is the simulated deformation,  $v_{tip}^0$  is the theoretical solution,  $f_1$  is the simulated vibration frequency and  $f_1^0$  is the theoretical value.

### 3.2. Flexible plate in uniform channel flow

In this section, we validate the codes through a benchmark case of a wall-mounted flexible plate in uniform channel flow. Interactions between the fluid and plate are considered. Luhar & Nepf (2011) carried out a series of model experiments in the channel flow on a flexible plate, widely used to compare numerical or experimental results. To check the fidelity of our present numerical methodology, we compare our numerical results with those of Luhar & Nepf (2011).

In our present simulation, the setting of the computational domain is very similar to the water flume experiment in Luhar & Nepf (2011), see their figure 3. Based on this, the computational domain is  $40 \text{ cm} \times 16 \text{ cm} \times 16 \text{ cm}$  in length, width and height, respectively. The water depth in the channel is 16 cm. In the inlet, the incoming flow is a uniform velocity  $U_\infty$ , while the velocity condition is applied in the outlet. For the top and lateral walls, free-slip boundaries are adopted. The bottom is a no-slip boundary and the wall function developed by Werner & Wengle (1993) was used. The geometric parameters for the flexible plate are the length ( $l$ ) of 5 cm, width ( $b$ ) of 1 cm and thickness ( $h$ ) of 0.2 cm,

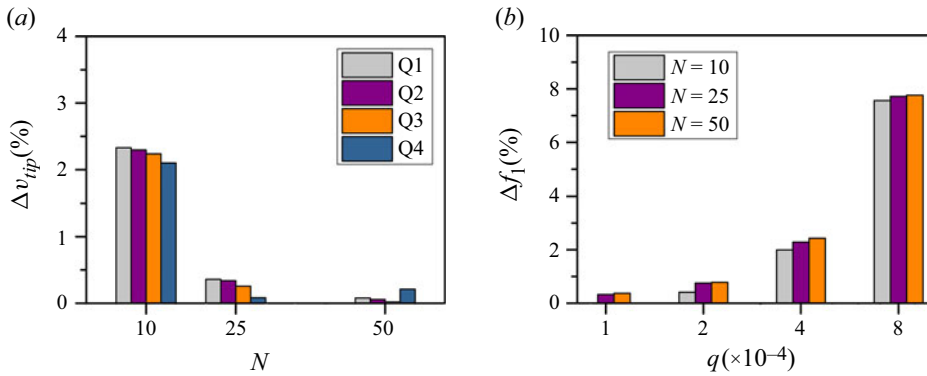


Figure 7. (a) The relative difference of the deformation at the free plate end versus the dimensions of the uniform loading, and (b) the relative difference of the vibration frequency of the plate with different elements versus the uniform loading.

respectively. The density of the flexible plate is  $0.678 \text{ g cm}^{-3}$ , the elastic modulus is  $5 \times 10^5 \text{ Pa}$  and the Poisson ratio is 0.4.

Before the validation, we first carry out a convergence test. A uniform mesh is applied around the flexible plate, and a large region is adopted to cover the possible motion of the plate. Outside this region, the stretched mesh with the constant ratio (not larger than 1.02) is adopted. Therefore, the total meshes is affordable in the present simulations. Four uniform meshes are selected, i.e.  $\Delta h/b = 0.2, 0.1, 0.0625$  and  $0.05$ . Here,  $h$  is the minimum mesh. The dimension ( $dx_s$ ) of the solid element is the same as the minimum mesh adopted. The fluid time step ( $dt_f$ ) for each situation is smaller than the critical time step ( $dt_f^0$ ) calculated through the equation below

$$dt_f^0 = \frac{\min(dx_f, dx_s)}{\sqrt{E/\rho_s} + 2U_\infty}, \quad (3.2)$$

where  $dx_f$  is the fluid mesh,  $dx_s$  is the dimension of the solid element,  $E$  is Young's modulus,  $\rho_s$  is the solid (or structure) density and  $U_\infty$  is the incoming flow velocity. The Reynolds number is  $Re_b = 1600$  when the width ( $b$ ) of the plate is used as the characteristic length.

Figure 8(a) compares the simulation results and those ( $D_x/b = 2.14$ ,  $D_z/b = 0.59$  and  $C_d = 1.03$ ) of model experiments in Luhar & Nepf (2011) under different mesh spacings. Here,  $D_x$  is the deflection of the plate at the free end in the streamwise direction,  $D_z$  is the height reduction of the plate at the free end and  $C_d$  is the drag force because of the flow around the vegetation. It is seen that the relative difference between the present simulation and the experiments of Luhar & Nepf (2011) becomes lower as the mesh is finer. When the mesh is no larger than  $\Delta h/b = 0.0625$ , the relative errors for  $D_x/b$  and  $C_d$  are lower than 1 % and smaller than 6 % for  $D_z/b$ . Thus, our numerical results agree well with the experiments of Luhar & Nepf (2011), suggesting a high fidelity of the present numerical methodology. Further, the mesh with  $h/b$  smaller than 0.0625 is an appropriate choice for our following simulations.

The incoming flow velocities, including  $U_\infty = 3.6, 11.0, 16.0$  and  $27.0 \text{ cm s}^{-1}$ , are simulated and compared with the experiments in Luhar & Nepf (2011) for further validation. The mesh with  $\Delta h/b = 0.0625$  is adopted. Figure 8(b) compares the drag force ( $F_d$ ) acting on the plate of the present simulation with both model predictions and experiment results. It is seen that the present simulation results are well matched with those

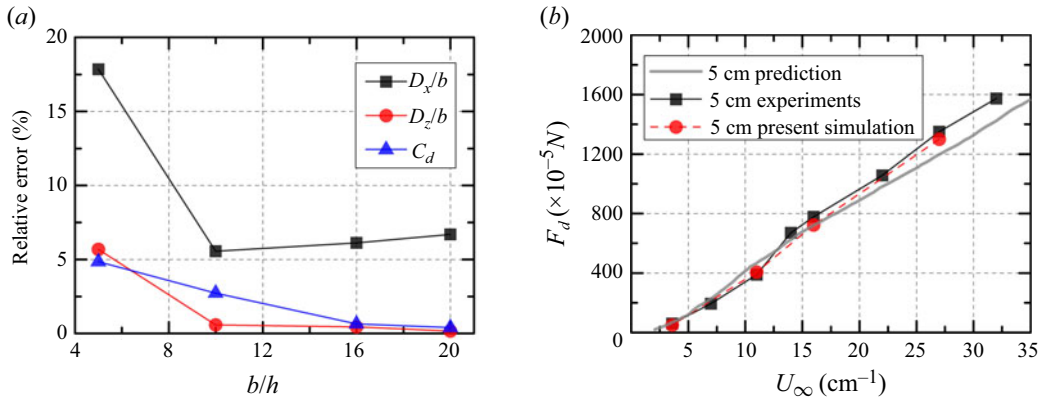


Figure 8. (a) The relative errors in hydrodynamic forces with different  $b/h$  values and (b) comparison of the drag force with prediction values and experimental results in Luhar & Nepf (2011).

in the experiments. This again indicates that our present methodology has high fidelity in simulating flexible plates in uniform channel flow.

### 3.3. Flexible stem under uniform loading

In this section, the deformation, including the tip position in the  $x$  and  $z$  directions and inclination angle of the chord line (i.e. between the tip and root) and horizontal line of a wall-mounted stem under uniform loading, is investigated and verified against the theoretical value, see figure 9(a). The aspect ratio is  $AR = 10$  and the uniform loading  $q$  is given according to the drag coefficient on the rigid stem. Figure 9(b–d) compares our simulation results with the theoretical value. It shows a good agreement for all three deformation quantities, thus suggesting a high fidelity.

As shown in figure 9(b,c), the tip position in either direction is dominated by stem stiffness while it is independent of  $Re$ . With increasing  $K$ ,  $x_{tip}/l$  decreases while  $h_{tip}/l$  increases gradually, corresponding to the state changing from upright to lodging. However, when  $\lg(K) > 0$ ,  $h_{tip}/l$  remains almost constant while  $x_{tip}/l$  decreases approximately linearly when the log–log coordinate is used. When  $\lg(K) < -3$ ,  $h_{tip}/l$  follows the relationship  $h_{tip}/l \sim K^{1/3}$ . This relationship was reported in Luhar & Nepf (2011).

As shown in figure 9(d), the inclination angle  $\theta$  grows with  $K$ , following the theoretical line. When  $K$  is large, the stem maintains upright, thus  $\theta \approx 90^\circ$ ; while  $K$  is extremely small, the stem maintains nearly parallel to the wall,  $\theta$  approaches  $0^\circ$ , indicating a lodging state.

### 3.4. Dynamics of a flexible filament in uniform flow

In this section, we validate the dynamics of a flexible filament by comparing our simulation results with those in Zhang *et al.* (2020). The computation domain and parameter settings are the same as those in Zhang *et al.* (2020). Two cases are selected: one is at  $\gamma = 0.008$  and the other is at  $\gamma = 0.004$ , with  $\beta$  and  $Re$  being constant at 1.0 and 400, respectively. Here,  $Re = U_\infty L/\nu$ ,  $\beta = \rho_s \delta_1/\rho_f L$  and  $\gamma = B/\rho_f U_\infty^2 L^3$ , where  $B$  is the bending rigidity,  $L$  is the length of the filament,  $\rho_s$  is the filament density and  $\delta_1$  is the thickness of the filament.

The time history of the inclination angle ( $\theta$ ) is plotted to check the consistency of the filament dynamics. Figure 10(a,c) shows the comparison of our simulation results with those in Zhang *et al.* (2020). Note that the results in figure 10(a,c) are using the mesh



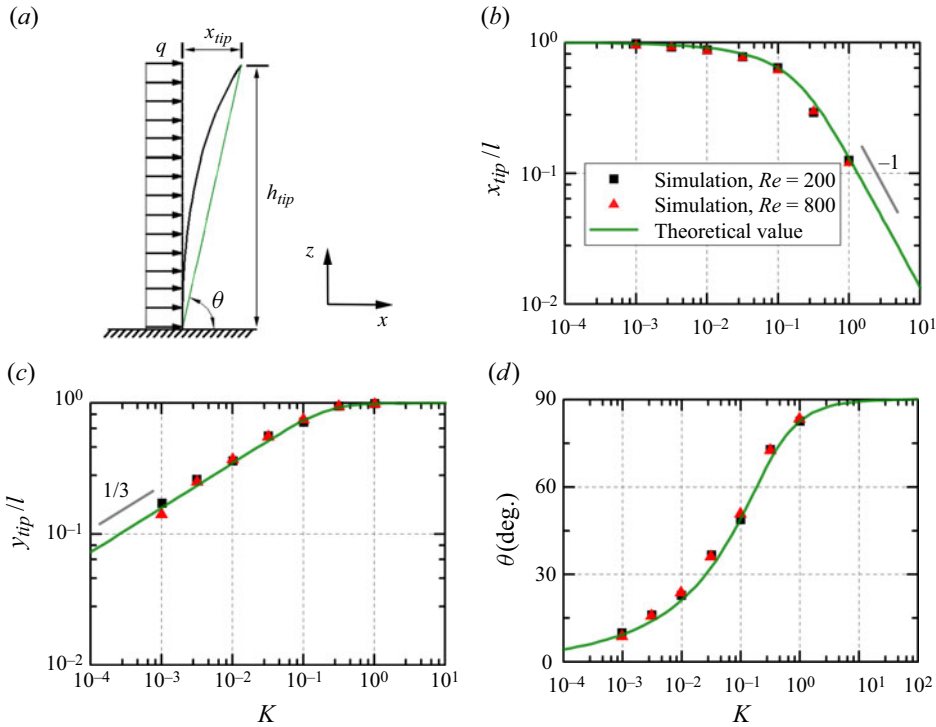


Figure 9. (a) Schematic of a wall-mounted flexible stem and deformation quantities, (b,c) the tip position in the  $x$  and  $z$  directions with  $K$ , and (d) the inclination angle  $\theta$  with  $K$ . The theoretical value is superimposed for comparison.

resolution of  $1/8$ . It is seen that our present simulation agrees well with those in Zhang *et al.* (2020) for the two cases. However, differences are also observed. For the first case (i.e.  $\gamma = 0.008$ ), the dominant frequency of the angular oscillation is slightly smaller than that in Zhang *et al.* (2020). For the second case (i.e.  $\gamma = 0.004$ ), the filament is much closer to the wall and the dynamics of the filament is influenced by the mesh resolution near the wall. The slight difference is at the smaller peaks of the angular oscillation. The mesh convergence is also shown in figure 10(b,d). For the first case, the angular oscillations for the meshes of  $1/16$  and  $1/32$  are well matched. This indicates that the mesh of  $1/16$  is appropriate for the present simulation. However, for the second case, the angular oscillation is convergent when the mesh is not coarser than  $1/32$ , see figure 10(d). This means that the latter case requires a finer mesh. For a more flexible filament, its tip goes much closer to the wall, and accordingly, it requires a finer mesh to deal well with the collision process. We also check the influence of the non-dimensional time step (not shown here). To achieve a convergent result, in our present simulation significantly small time steps are adopted. The difference observed on halving the adopted time step is insignificant.

### 3.5. The non-dimensional time step for a wall-mounted stem in uniform flow

In this section, we check the influence of the non-dimensional time step in the simulation of a wall-mounted flexible stem. The aspect ratio is constant at  $AR = 10$  and the Reynolds number is  $Re = 400$ . As shown in table 1, by reducing the non-dimensional time step by half, the largest difference for  $A_x$  is only 3.2 %.

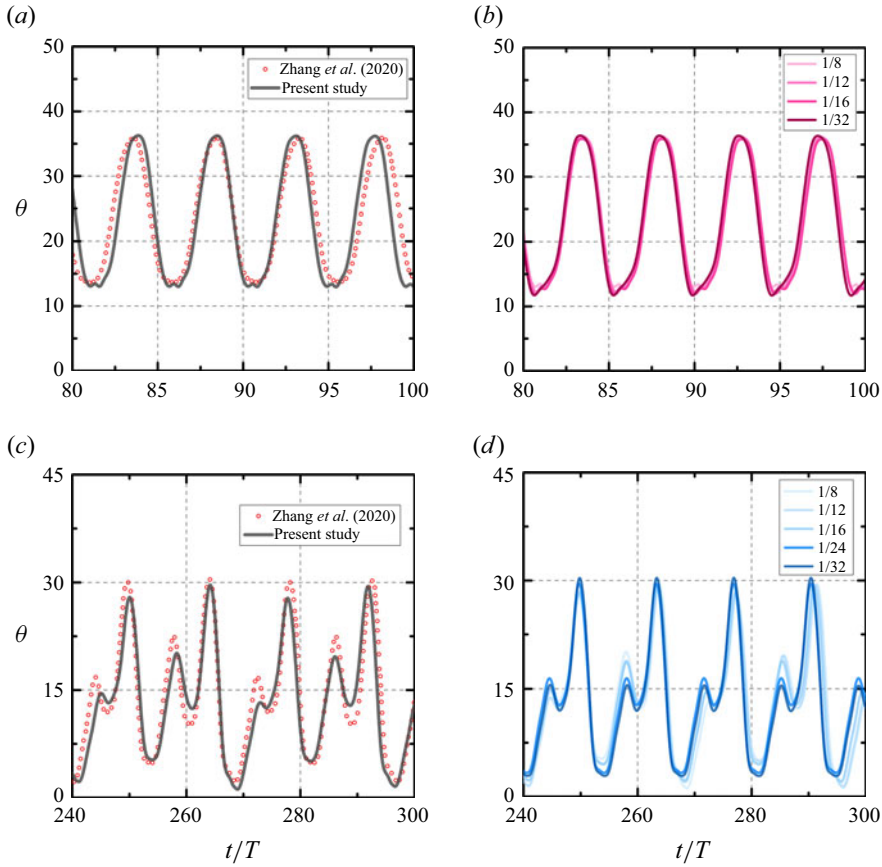


Figure 10. (a,c) Comparison of the time history of the inclination angle ( $\theta$ ) of the present study with Zhang *et al.* (2020), and (b,d) time history of the inclination angle ( $\theta$ ) at different grid spacings. (a,b) Are for the case of  $Re = 400$  and  $\gamma = 0.008$ , and (c,d) are for the case of  $Re = 400$  and  $\gamma = 0.004$ .

$\Delta t U_\infty / D$	$A_x$	$A_y$	$A_z$	$f$
$1.6 \times 10^{-4}$	0.064	0.962	0.031	0.132
$8 \times 10^{-5}$	0.062	0.984	0.032	0.128
Difference (%)	3.2	3.1	3.1	3.1

Table 1. Comparison of the oscillation amplitudes in three directions and dominant frequency in the transverse direction at different non-dimensional time steps for a wall-mounted flexible stem at  $Re = 400$  and  $\lg(K) = -0.5$ .

### 3.6. Other validation

Another validation, such as flow over a rigid circular cylinder in unbounded flow with the  $Re$  up to 1000, has been provided in our previous work (Chen *et al.* 2022). The mesh settings in the present study are approximately the same as those adopted in the direct numerical simulation. The convergence analysis of the grid spacing and non-dimensional time step has been conducted in our previous work.

#### 4. Numerical set-up for a wall-mounted stem in uniform flow

In this section, we present the numerical set-up employed in this study and explain the practical rationale behind its design. It is noted that only dimensionless quantities are employed in our numerical simulations of a wall-mounted stem.

- (i) Cross-section of the wall-mounted stem: numerous natural applications feature a wall-mounted configuration, such as trees in a forest, seaweed on the seafloor, cilia on membranes and bivalves inhabiting riverbeds. These structures exhibit a variety of shapes, including circular, rectangular, plate-like and thin filamentous forms. In this study, we aim at the 3-D flow characteristics and dynamic response of a wall-mounted stem. The circular cross-sectional shape is chosen as it is more representative and rotational symmetry and thus insensitive to incoming flow directions.
- (ii) Aspect ratio: the aquatic plants generally have large aspect ratios (ARs), ranging from 10 to 100 (Ghisalberti & Nepf 2002; Luhar *et al.* 2010; Luhar & Nepf 2011). To save computational resources and conduct more simulation cases, a lower end of AR (= 10) is adopted in this study.
- (iii) Reynolds number: the flow velocity at the location of the aquatic plants is strongly influenced by factors such as the topography, ocean currents, tides and geographical location. Near the coast, tides play a significant role, with flow velocity typically ranging from 0.1 to 1 m s<sup>-1</sup>. In contrast, plants in the deep sea are primarily affected by ocean currents, where the flow velocity is generally more stable, typically within the range of 0.01–0.2 m s<sup>-1</sup>. The characteristic width of these plants is of the order of 1 cm (Luhar *et al.* 2010; Luhar & Nepf 2011). Accordingly, the Reynolds number  $Re$  ( $= U_\infty D/\nu$ ) based on the width (or diameter) is in the range of  $10^2$ – $10^4$ . In a coastal system, a condition with  $Re \gtrsim 200$  is common (Munson, Young & Okiishi 1990; Leonard & Luther 1995). However, in a freshwater system not exposed to strong tides, a condition with  $Re \lesssim 200$  is more typical. For  $Re \lesssim 200$ , the wake production is negligible and turbulent components are greatly reduced (Ghisalberti 2000). A moderate  $Re$  range is selected, i.e.  $Re = 200$ – $1000$ , covering the conditions from river to coast, which is obtained by setting different initial  $U_\infty$ .
- (iv) Stiffness ratio: for flexible stems, the stiffness ratio, representing the ratio of the elastic force and inertia force, is introduced, defined as  $K = 1/Ca$ . Here, the Cauchy number  $Ca$  is defined as  $Ca = 0.5\rho_f D l^3 U_{ref}^2 / EI$ , where  $\rho_f$  is the fluid density,  $l$  is the stem length,  $D$  is the stem diameter,  $E$  is Young's modulus,  $I$  is the cross-section moment of inertia, defined as  $I = \pi D^4/64$  for the circular cross-section, and  $U_{ref}$  is the incoming flow velocity. For a single stem,  $U_{ref} = U_\infty$ . For aquatic plant, the stiffness ratio is in the range of  $K = 2.0 \times 10^{-4}$  –  $3.0 \times 10^2$  (Luhar & Nepf 2011), corresponding to  $\lg(K) = -3.59$  –  $2.48$ . Our simulation indicates that, when  $\lg(K) > 0$ , the dynamic response is insignificant. In this study, eight different stiffness ratios, i.e.  $\lg(K) = -3.5, 3.0, \dots, 0$  with an increment of 0.5, are applied for each  $Re$ .
- (v) Density of the stem: the density  $\rho_s = 1.0$  is applied, which is a typical density of aquatic plants (Gaylord & Denny 1997; Bradley & Houser 2009; Luhar & Nepf 2011; Vettori & Nikora 2018; O'Connor & Revell 2019).
- (vi) Structural damping: in this study, the structural damping coefficient ( $\zeta$ ) is set as zero. Thus, the flexible stem experiences the strongest oscillation.
- (vii) Computational domain: as shown in figure 4(d), the distance is  $10D$  from the stem centre to the inlet and  $30D$  to the outlet. The stem to each side of the lateral

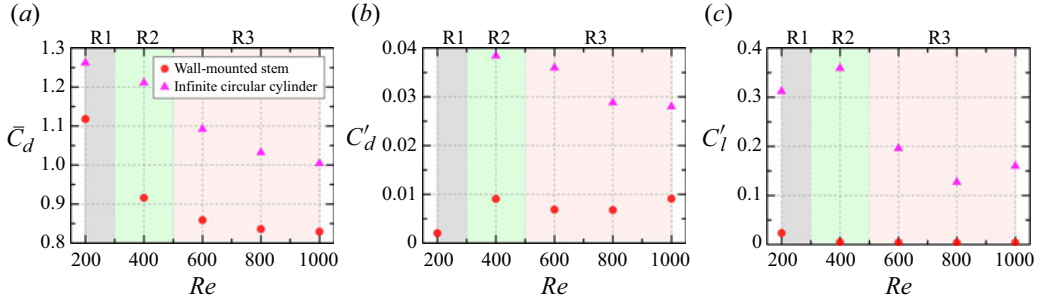


Figure 11. Dependence of (a) mean drag ( $\bar{C}_d$ ), (b) fluctuating (r.m.s.) drag ( $C'_d$ ) and (c) fluctuating (r.m.s.) lift ( $C'_l$ ) coefficients on  $Re$  ( $= 200 - 1000$ ). The triangle symbols in (a,c) represent the results of flow over an infinite circular cylinder from Jiang and Cheng (2021). The results in (b) are provided by H. Jiang (personal communication). Here, R1, R2 and R3 denote different regimes based on the features of lift spectra and the vortex dynamics.

boundary is  $8D$  and the height in the  $z$ -direction is  $16D$ . The value  $\Delta z/l = 1/16$  is applied. At the stem position, the boundary layer thickness ( $\delta/D$ ) is low, varying from 1.1 to 0.5 within  $Re = 200-1000$ . The computational domain is discretised by a non-uniform Cartesian grid with a resolution of  $1536 \times 512$ . The non-dimensional grid spacing in the  $x-y$  plane is  $1/32$ . A total of 160 points are applied in the VFIFE method.

- (viii) Boundary conditions: a Dirichlet-type boundary is adopted at the inflow, and a Neumann-type boundary is employed at the outflow. The top and bottom walls are free slip and no slip, respectively, and the free-slip boundary condition is adopted at two lateral boundaries.
- (ix) Non-dimensional time step and time span: in our present simulation, both the time span and time step depend strongly on  $Re$  and  $K$ . To provide a convergent result, the non-dimensional time step is of the order of  $10^{-4}$  or  $10^{-5}$ , and the corresponding Courant–Friedrichs–Lewy number is of the order of 0.01 or 0.001. It is found that the non-dimensional time span is closely associated with the response type. For periodic or regular response, the time span may reach  $\sim 1000$ , while for chaotic response it may reach  $\sim 3000$ . It should be pointed out here that, although the time span is already long, some cases are still unstable, such as the case at  $Re = 200$  and  $\lg(K = -2.0)$  where slow flapping behaviour occurs.

## 5. Wall-mounted rigid stem in uniform flow

This section reports the characteristics of the hydrodynamic forces, vortex shedding frequency and flow structures of a wall-mounted rigid stem to provide some primary understanding and to facilitate further comparison with the flexible stem.

### 5.1. Statistics of fluid forces and vortex shedding frequency

Figure 11 shows the vertically averaged fluid forces on the rigid stem at  $Re = 200 - 1000$ . Here, the drag and lift coefficients are defined as  $C_d = 2F_d/\rho U_\infty^2 Dl$  and  $C_l = 2F_l/\rho U_\infty^2 Dl$ , respectively. As shown in figure 11(a), the mean drag coefficient ( $\bar{C}_d$ ) is 1.12 at  $Re = 200$  and gradually decreases as  $Re$  increases. The  $\bar{C}_d$  values for a circular cylinder in an unbounded flow (represented by triangular symbols) are slightly higher than those for the wall-mounted case. This discrepancy arises because, in the wall-mounted case: (i) the oscillating shear layers near the junction are suppressed by the wall, and

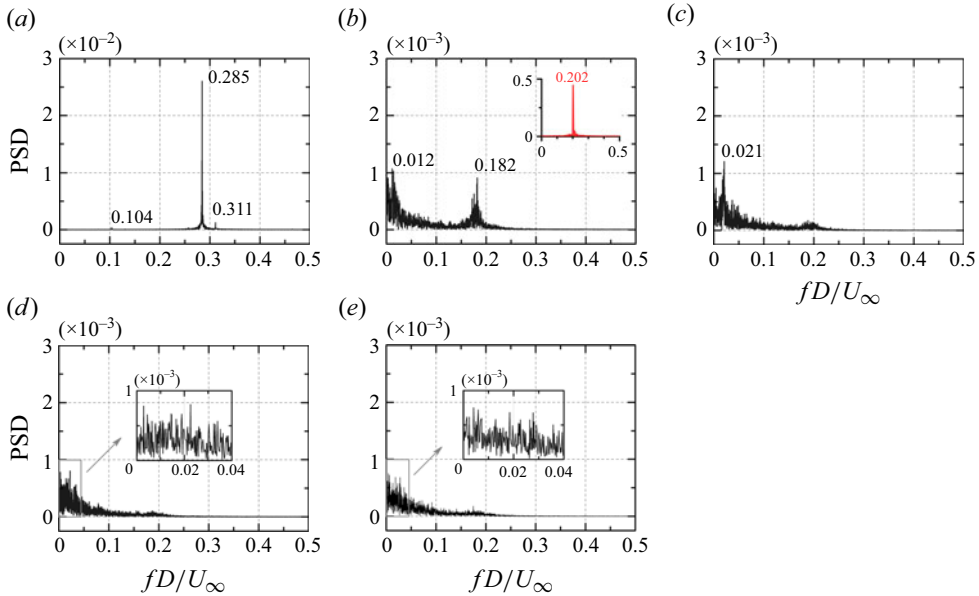


Figure 12. Power spectral density (PSD) of the vertically averaged lift coefficient of a wall-mounted rigid stem within  $Re = 200 - 1000$ . Panels show (a)  $Re = 200$ , (b)  $Re = 400$ , (c)  $Re = 600$ , (d)  $Re = 800$  and (e)  $Re = 1000$ . The inset in (b) shows the spectrum of the lift coefficient of an infinite circular cylinder at  $Re = 400$ .

(ii) the free end delays flow separation, resulting in a less negative wake pressure (Luo, Gan & Chew 1996). As discussed later, the downwash flow from the free end pushes the shear layers away from the stem base, contributing to the reduction in  $\bar{C}_d$ .

The r.m.s. drag coefficient ( $C'_d$ ), shown in figure 11(b), exhibits a different behaviour with  $Re$ . At  $Re = 200$ ,  $C'_d$  is approximately zero (0.001). For higher  $Re$  values,  $C'_d$  stabilises around 0.08, which is significantly higher than at  $Re = 200$ . This suggests a fundamental difference in the vortical structures between  $Re = 200$  and  $Re > 200$ . The  $C'_d$  values for an infinite circular cylinder at the corresponding  $Re$  are also plotted in figure 11(b). It is seen that the  $C'_d$  values in triangular symbols are much higher than those for the wall-mounted case, implying that the vortical structures near the free end and junction suppress shear layer fluctuations (Baban, So & Otugen 1989; Wang & Zhou 2009; Kumar & Tiwari 2019).

Due to the rotational symmetry of circular cross-section, the time-averaged lift coefficient ( $\bar{C}_l$ ) is zero and will not be discussed further. As shown in figure 11(c), the r.m.s. lift coefficient ( $C'_l$ ) for the wall-mounted stem is relatively large at  $Re = 200$ , with a value of 0.023. However, at higher  $Re$ ,  $C'_l$  stabilises at approximately 0.005. The transitions for  $C'_d$  and  $C'_l$  from  $Re = 200$  to  $Re > 200$  exhibit contrasting behaviours, highlighting the influence of different vortical structures in these two  $Re$  clusters. These two  $Re$  clusters will be analysed further to explore the roles of different flow structures in the transition. The  $C'_l$  values for the infinite circular cylinder, represented by triangular symbols in figure 11(c), are much higher due to the reduced fluctuations in the shear layers of the wall-mounted stem.

The vortex shedding frequency is a key indicator of flow physics and is significantly influenced by the vortex dynamics at both the free end and the junction (Liu, So & Cui 2005; Yauwenas *et al.* 2019). Figure 12 shows the spectra of the vertical-averaged lift coefficient at  $Re = 200 - 1000$ , representing the vortex shedding frequency. As  $Re$

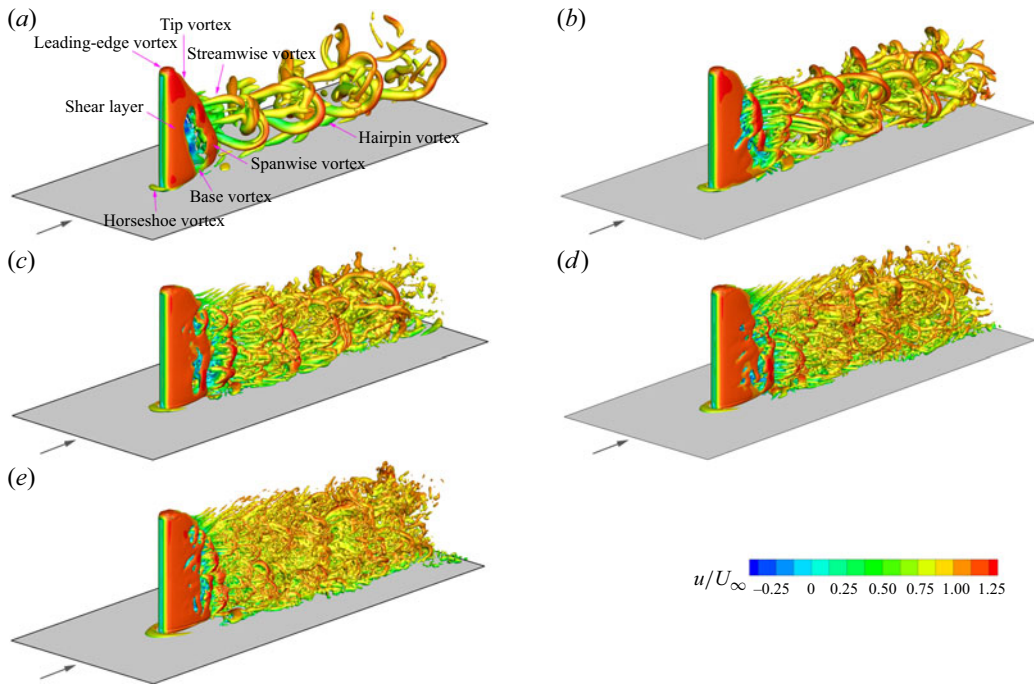


Figure 13. Three-dimensional vortical structures behind the wall-mounted rigid stem at (a)  $Re = 200$ , (b)  $Re = 400$ , (c)  $Re = 600$ , (d)  $Re = 800$  and (e)  $Re = 1000$ . The  $Q$ -criterion is adopted to visualise the vortex structures (Hunt *et al.* 1988), i.e.  $Q = 5, 20, 45, 80$  and  $125$  for panels (a–e). The arrow indicates the flow direction (i.e. from left to right).

increases, the spectral characteristics exhibit three distinct patterns. At  $Re = 200$ , three frequencies are observed, but two have trivial magnitudes, as shown in figure 12(a). The dominant frequency is  $f^* (= fD/U_\infty) = 0.285$ . However, at  $Re = 400$ , the dominant frequency decreases to  $f^* = 0.182$ , significantly lower than at  $Re = 200$ . Compared with the unbounded case, the dominant frequency is slightly lower, see the inset in figure 12(b). A secondary frequency,  $f^* = 0.012$ , is approximately one order of magnitude lower than the dominant one. At  $Re = 600$ , only one low frequency is detected at  $f^* = 0.021$ , as shown in figure 12(c). For  $Re = 800 - 1000$ , no dominant frequency is observed, as multiple low-frequency components below 0.03 exhibit comparable but weak magnitudes, see figure 12(d,e).

Based on the features of hydrodynamic forces and vortex shedding frequencies, the investigated  $Re$  can be categorised into three regimes. The first regime (R1) corresponds to  $Re = 200$ , where vortex shedding is periodic, and correspondingly, a regular lift spectrum appears. The second regime (R2) occurs at  $Re = 400$ , where both low and high frequencies appear due to different vortical structures. The third regime (R3) spans at  $Re = 600 - 1000$ , where only low-frequency components are present. A slight distinction exists between  $Re = 600$  and  $Re = 800 - 1000$  in that the lift spectrum becomes chaotic at higher  $Re$ . These variations are linked to the evolution of different 3-D vortical structures.

### 5.2. Details of the 3-D vortical structures

The vortical structures in the studied  $Re$  range are shown in figure 13. Since the AR exceeds the critical value (Bourgeois *et al.* 2011, 2012), the shear layer from the front side is reattached onto the free-end surface due to flow reversal (Pattenden *et al.* 2005;



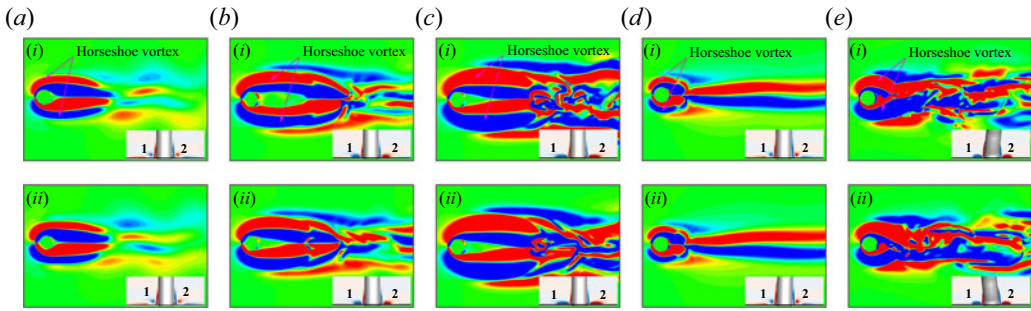


Figure 14. The vorticity field of a wall-mounted stem at the vertical position of  $z/D = 0.1$ . (a–c) For a rigid stem and (d, e) for a flexible stem. Panels show (a)  $Re = 200$ , (b)  $Re = 400$ , (c)  $Re = 600$ , (d)  $Re = 200$  and  $\lg(K) = -0.5$  and (e)  $Re = 600$  and  $\lg(K) = -2.0$ . The HV in each plot is marked; (i) and (ii) at different instants. The legs of the HV system, visualised by the  $x$ -vorticity at  $x/D = 0$ , are marked in the subplot.

Krajnovic 2011; Essel *et al.* 2021). The leading-edge vortex emerges at the free end surface, while near the bottom, horseshoe vortices form upstream of the stem, wrapping around its sides and trailing behind it (Hussein & Martinuzzi 1996; Simpson 2001; Wang & Zhou 2009; Chang *et al.* 2017, 2020) due to the adverse pressure gradient. These vortices tend to drive the flow downward inside its vortical trails. Figure 14 shows the horseshoe vortex (HV) system circling the stem base at a vertical position of  $z/D = 0.1$ . Within the studied  $Re$ , the HV system is characterised by a single necklace vortex, as marked in figure 14. In the current simulation, both  $Re$  and  $\delta/D$  increase simultaneously as the incoming flow velocity rises. As expected, the HV grows with increasing  $Re$ , exhibiting greater strength and a longer extension into the wake. This suggests that the dynamics of the HV system is affected by  $Re$ , the characteristics of the upstream boundary layer and the shape of the cylinder (Baker 1979; Seal *et al.* 1995). As shown in figure 14(a), the HV at  $Re = 200$  remains nearly constant, with weak interactions with the two side shear layers and no noticeable amalgamation. However, at higher  $Re$  ( $= 400 - 600$ ), the HV legs extend further downstream, see figure 14(b,c). At  $Re = 400$ , the HV system encircles the two side shear layers, and their interactions intensify. In the wake, vortices shed from the HV system and the two side shear layers mix together, and amalgamation occurs. At  $Re = 600$ , the interactions between the HV system, the shear layers on either side of the stem and the resulting vortices become more pronounced. The conditions at  $Re = 800 - 1000$  are very similar to those at  $Re = 600$  and are therefore not shown. The HV system could be either laminar or turbulent. The laminar type is typically classified into five, transiting from steady to periodic by increasing  $Re$  and/or  $\delta/D$  (Greco 1990; Seal *et al.* 1997; Wei, Chen & Du 2001; Kirkil & Constantinescu 2012). In the present simulation, the HV system remains laminar, with a steady necklace vortex persisting at  $Re = 200 - 1000$  due to the combined effects of lower  $Re$  and a thin  $\delta/D$  (Wei *et al.* 2001). In Kirkil & Constantinescu (2012), where the boundary layer thickness is  $\delta/D \cong 0.6$ , the laminar HV system transitions from steady to periodic oscillating and then to periodic breakaway as  $Re$  increases. In the flexible case, the HV system also remains steady but is significantly influenced by the redistribution of vortical structures. As will be shown later, the flexible stem experiences stronger vortex shedding near the tip due to larger amplitudes and significant deformation. At  $Re = 200$ , the HV system remains stable but its vortex legs extend a shorter distance downstream compared with the rigid stem, see figure 14(d). A similar behaviour is noticed at  $Re = 600$ , see figure 14(e). It should be noted that as the stem becomes more flexible, the HV system is strongly affected because the two side shear layers (or separated vortices) move closer to the wall, influencing the HV system's

development. More details of the interactions between different vortex structures will be discussed later.

The evolution of 3-D vortical structures at  $Re = 200$  is shown in [figure 13\(a\)](#). Due to the high AR, the shear layers are allowed to develop and separate from the stem (Fröhlich and Rodi, 2004; Pattenden *et al.* 2005; Tsutsui 2012). The spanwise vortices exhibit a slanted arrangement with an inclination angle of roughly  $32.6^\circ$  (measured between the vertical axis and the slanted shear layer line) due to the influences of downwash flow from the free end (Lee 1997; Fröhlich and Rodi, 2004). In the near wake, the spanwise vortices are significantly bent and stretched. Upwash and downwash flow entrain free-stream flow into the wake, pushing the spanwise vortices away from the centreline. Meanwhile, the streamwise vortices gradually develop. As a result of vortex twisting and interaction, the deformation of the spanwise and streamwise vortices becomes more evident further downstream. However, the interactions between these vortices weaken as they move apart. Compared with  $Re = 200$ , the 3-D vortical structures at  $Re = 400$  are more complex, featuring finer-scale vortices. Despite these differences, similarities remain, such as the presence of downwash flow, see [figure 13\(b\)](#). At this  $Re$ , the spanwise vortices take over a longer length, but their formation region is larger near the wall. Near the free end, spanwise vortices are absent, while streamwise vortices develop more quickly due to increased flow velocity. As a result, vortex interactions intensify, leading to faster dissipation.

At  $Re = 600$ – $1000$ , the vortex dynamics is characterised by finer-scale vortices. As shown in [figure 13\(c–e\)](#), spanwise vortices separate from the stem simultaneously and remain approximately parallel. Compared with the lower  $Re$  cases (200–400), the finer-scale spanwise vortices exhibit more irregular behaviour in the near wake, as indicated by significantly low dominant frequencies. Similarly, the streamwise vortices are smaller in scale and mix with the spanwise vortices (Zhang *et al.* 2021), leading to faster dissipation. Although the downwash flow persists, it is considerably weaker, as indicated by the formation of spanwise vortices closer to the free end.

[Figure 15](#) shows the  $z$ -vorticity contours at different vertical positions. It is evident that vortex shedding varies significantly along the length within the studied  $Re$  range. At  $Re = 200$ , vortex shedding is regular near the junction. As shown in [figure 15\(a–i\)](#), the vortex shedding in this region (i.e.  $z/D = 0.5$ ) is characterised by the formation of horseshoe and hairpin vortices in the wake. The hairpin vortex comes from disturbances in the stretched vortices affecting the boundary layer over the stationary wall, a behaviour similar to the bypass transition observed over a circular cylinder (He *et al.* 2017). The shear layers on both sides extend further downstream, and the separated vortices gradually dissipate in the far wake. At the middle plane (i.e.  $z/D = 5.0$ ), vortices shed alternately from both sides of the stem. In the near wake, they appear nearly identical, apart from their opposite rotation directions, see [figure 15\(a–ii\)](#). Further downstream, these vortices become increasingly irregular due to the bending and twisting of spanwise vortices and the emergence of stretched streamwise vortices, leading to a broader wake. Higher up, i.e.  $z/D = 7.5$ , the shear layers weaken, and fluctuations of shear layers occur farther downstream, with dissipation occurring more rapidly than at the middle plane, see [figure 15\(a–iii\)](#). Near the free end, i.e.  $z/D = 9.5$ , the shear layers on both sides remain stable, with no visible vortices in the wake, forming a symmetric wake, see [figure 15\(a–iv\)](#).

At  $Re = 400$ , vortex strength increases compared with  $Re = 200$ . As shown in [figure 15\(b–i\)](#), the HV near the junction is more intense and extends farther downstream. Compared with  $Re = 200$ , the shear layers on both sides of the stem extend further downstream. The hairpin vortex appears in the near wake but exhibits greater irregularity. Interaction between the hairpin vortex and spanwise vortices occurs where the spanwise vortices separate. At the midspan (i.e.  $z/D = 5.0$ ), the vortex shedding pattern is similar to

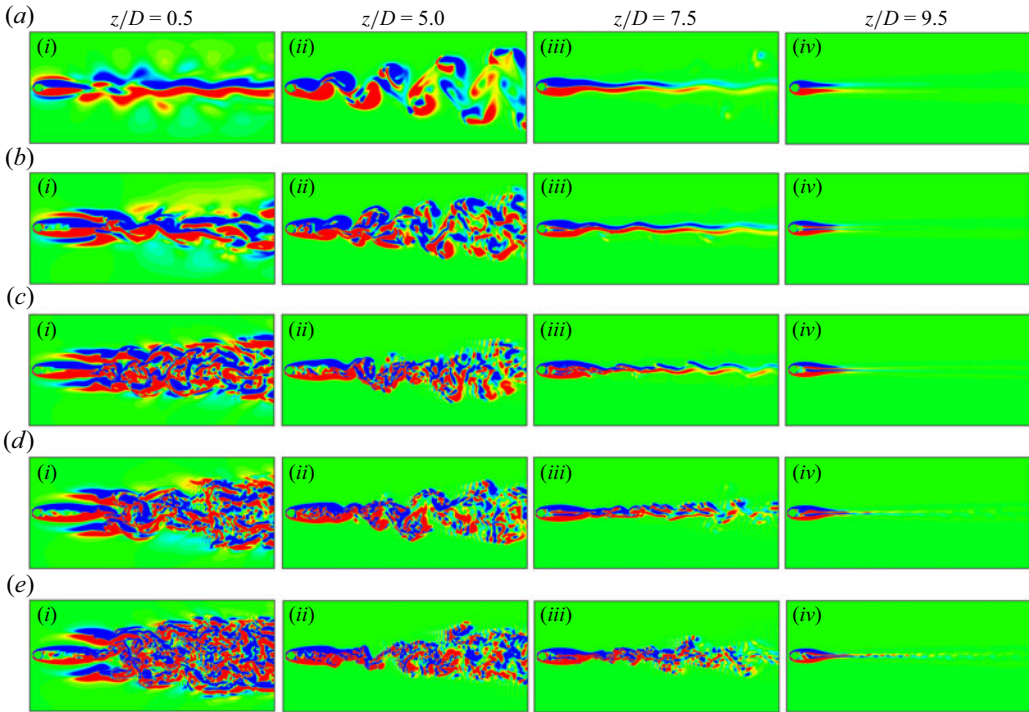


Figure 15. The vorticity contours ( $\omega_z^* = (D/2U_\infty)((\partial v/\partial x) - (\partial u/\partial y))$ ) of a single stem at several vertical positions. Panels show (a)  $Re = 200$ , (b)  $Re = 400$ , (c)  $Re = 600$ , (d)  $Re = 800$  and (e)  $Re = 1000$ .

that at  $Re = 200$ , although the vortices are slightly smaller, see [figure 15\(b-ii\)](#). In the near wake, vortices become finer and more irregular before the wake widens. At  $z/D = 7.5$ , weak fluctuations in the shear layers are observed, see [figure 15\(b-iii\)](#). Further downstream, the shear layers thin out due to dissipation. Near the free end, i.e.  $z/D = 9.5$ , the shear layers remain stable, with no vortices shed into the wake, see [figure 15\(b-iv\)](#). Compared with  $Re = 200$ , the downwash flow at  $Re = 400$  is stronger but extends over a shorter length.

As shown in [figure 15\(c-e\)](#), the vortex shedding patterns at the same vertical position remain similar for  $Re = 600 - 1000$ . As  $Re$  increases, vortices become stronger but more irregular. As shown in [figure 15\(c-i, d-i, e-i\)](#), the HV intensifies, and its legs extend further downstream. Vortex shedding occurs at a relatively shorter downstream position with increasing  $Re$ . The formed vortices subsequently interact with the HV. Further downstream, the vortices become finer and dissipate more quickly, leading to a wider wake. At midspan, vortex formation shifts further downstream compared with the low  $Re$  case, see [figure 15\(c-ii, d-ii, e-ii\)](#). At higher vertical position, i.e.  $z/D = 7.5$ , the wake narrows significantly. Near the free end, the shear layers are slightly unstable with small vortices formed in the wake for  $Re = 800 - 1000$ , see [figure 15\(c-iv, d-iv, e-iv\)](#).

### 5.3. The downwash and upwash flow

In §§ 5.1 and 5.2, we discussed the effects of downwash and upwash flow on the vortex dynamics. [Figure 16](#) shows side views of these flows. For each  $Re$ , the separated flow from the free end enters the near wake at a nearly constant angle relative to the streamwise direction ([Krajnovic 2011](#)). As shown in [figure 16\(a\)](#), at  $Re = 200$ , the flow from the free end moves downward directly along the bottom (i.e.  $x/D = 1.0$ ), indicating that the

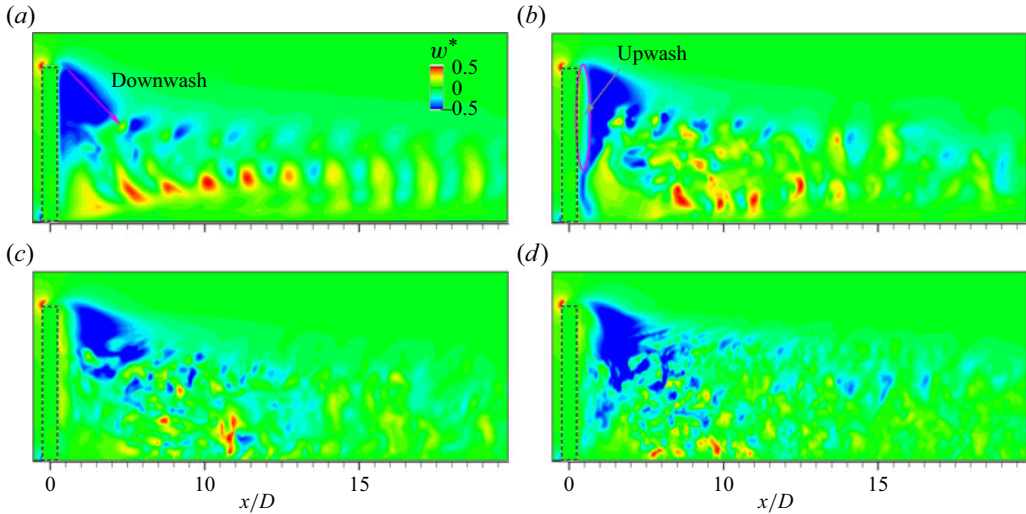


Figure 16. Instantaneous vertical velocity ( $w^*$ ) at the  $y (= 8D)$  plane for  $Re = 200$ – $600$ . Panels show (a)  $Re = 200$ , (b)  $Re = 400$ , (c)  $Re = 600$  and (d)  $Re = 1000$ . Flow is from left to right. The rectangle in each plot indicates the stem position.

downwash flow initiates immediately behind the stem but weakens gradually. Beyond  $x/D \geq 4.0$ , the downwash flow becomes nearly negligible.

At  $Re = 400$ , the downwash flow extends slightly farther downstream. As shown in [figure 16\(b\)](#), downwash begins just past the free end but primarily affects the lower part of the stem at  $x/D = 1.0$ . A slight upward flow is observed at the upper part, indicating the presence of upwash flow. The downwash flow weakens quickly and disappears around  $x/D = 8.0$ .

At  $Re = 600$ , the downwash flow behaves similarly, as shown in [figure 16\(c\)](#). Behind the stem, an upward flow is observed, pushing the downwash flow further downstream. Between  $x/D = 4.0$  and  $8.0$ , the downwash flow weakens but spreads toward the wall. In contrast, at  $Re = 800$ – $1000$ , the downwash flow reaches the wall, whereas at  $Re = 600$ , it does not, see [figure 16\(c,d\)](#).

Upwash flow appears at  $Re = 400$ – $1000$ , where it coexists with downwash flow. At  $Re = 600$ , the upwash flow originates from the junction and is associated with the development of the near-wake base vortex (Etzold & Fiedler 1976; Essel *et al.* 2021). As indicated in [figure 1](#), the base vortex consists of a pair of streamwise counter-rotating vortices near the base of the stem, influenced by  $Re$  and  $\delta/D$  (Sumner *et al.* 2004; Wang *et al.* 2006; Wang & Zhou 2009). As shown in [figure 16\(c,d\)](#), the upwash flow intensifies with increasing  $Re$ . However, at  $Re = 400$ , the upwash flow is only present in the upper region (see [figure 16\(b\)](#)), exhibiting a different behaviour from higher  $Re$  cases.

#### 5.4. Three-dimensional wake instability comparison with the infinite cylinder case

In this section, we compare the 3-D wake instability of a wall-mounted cylinder with that of an infinite cylinder to deepen our understanding of the effects of the impermeable wall and free end. For flow past an infinite circular cylinder, the wake exhibits distinct patterns due to the presence of inherent 3-D wake instabilities (i.e. modes A and B) as  $Re$  increases from approximately 190 to 300 (Williamson 1996; Jiang *et al.* 2016). The transition from mode A to mode B has been well documented. Notably, mode A remains stable only for a short period before transitioning into a more stable pattern, mode A\*, which exhibits



significant dislocation. At  $Re \leq 220$ , mode  $A^*$  dominates, while modes  $A^*$  and B coexist in the range of  $230 \leq Re \leq 265$ . When  $Re \geq 270$ , mode  $A^*$  disappears, and mode B becomes the dominant instability. Modes  $A^*$  and B exhibit distinct characteristics. Mode  $A^*$ , induced by an elliptic instability of the primary vortex cores, features streamwise vortices that are out of phase between neighbouring braids. Due to spanwise waviness, the primary vortex cores become significantly stretched. In contrast, mode B, caused by the hyperbolic instability of the braid shear layer, exhibits an in-phase pattern. Compared with mode A, the primary vortices in mode B are more stable, with no noticeable spanwise waviness.

As discussed in § 5.2, the vortex dynamics of a wall-mounted cylinder is significantly altered by the presence of the impermeable wall and free end. A key feature of this configuration is the suppression of vortex formation near both the cylinder base and the free end. Consequently, the separation of the spanwise shear layers typically occurs in a slanted manner, see figure 13(a,b). Compared with the infinite cylinder case, the wake transition of the wall-mounted cylinder is influenced by additional factors, including  $Re$ ,  $AR$  and  $\delta/D$ . Kumar & Tiwari (2019) found that, at  $AR = 5$ , no vortex shedding occurs when  $Re \leq 100$ , indicating a symmetric wake structure. When  $Re \geq 150$ , spanwise vortex shedding emerges, with vortices transitioning into hairpin-like structures. The critical  $Re$  for the onset of vortex shedding increases as  $AR$  decreases (Saha 2013). It is expected that if the wall-mounted cylinder has a much larger  $AR$ , modes  $A^*$  (or A) and B would likely emerge. However, for a short cylinder, the wake structures are primarily governed by downwash and upwash flows (Zhu *et al.* 2017), resulting in a distinctly different flow behaviour.

In the present simulation, we observe two patterns of 3-D wake instabilities. As shown in figure 13(a), the streamwise vortices primarily result from the suppression of shear layer separation. In the near wake, the separated vortices undergo significant stretching before transitioning into the hairpin-like structures. At higher  $Re$  ( $= 400$ ), the formation of streamwise vortices resembles mode  $A^*$ . As shown in figure 13(b), streamwise vortices appear after the spanwise vortices separate from the shear layers, exhibiting large dislocations. The emergence of mode- $A^*$ -like instability is closely associated with slanted vortex shedding. However, in the near wake, the formed streamwise vortices undergo significant stretching, preventing the mode- $A^*$ -like vortices from persisting farther downstream. Additionally, mode B, which typically appears in an in-phase pattern, is absent in the wall-mounted case. This absence may be attributed to the slanted nature of vortex shedding.

It is important to note that the 3-D wake instabilities observed in this study apply specifically to the simulated conditions. Further investigation is needed to explore these phenomena in great detail.

## 6. Fluid–structure interaction of a wall-mounted flexible stem in uniform flow

In this section, we examine the behaviour of a wall-mounted flexible stem in uniform flow, focusing on shape deformation, stem response, vortex dynamics, hydrodynamic forces and the spectral characteristics of displacement. Key aspects are analysed, including the evolution of 3-D vortical structures, wake topologies and tip movements under varying stiffnesses. The aspect ratio is set at  $AR = 10$ , the Reynolds number ranges from  $Re = 200$  to 1000 and the stiffness ratio is  $\lg(K) = -3.5$ –0 with an increment of 0.5. As discussed in § 4, no structural damping is applied. In total, 40 LES are carried out. Notably, in certain cases, the stem response is highly chaotic, and no convergent state is reached even over a longer non-dimensional time span, i.e.  $tU_\infty/D \sim O(10^3)$ .

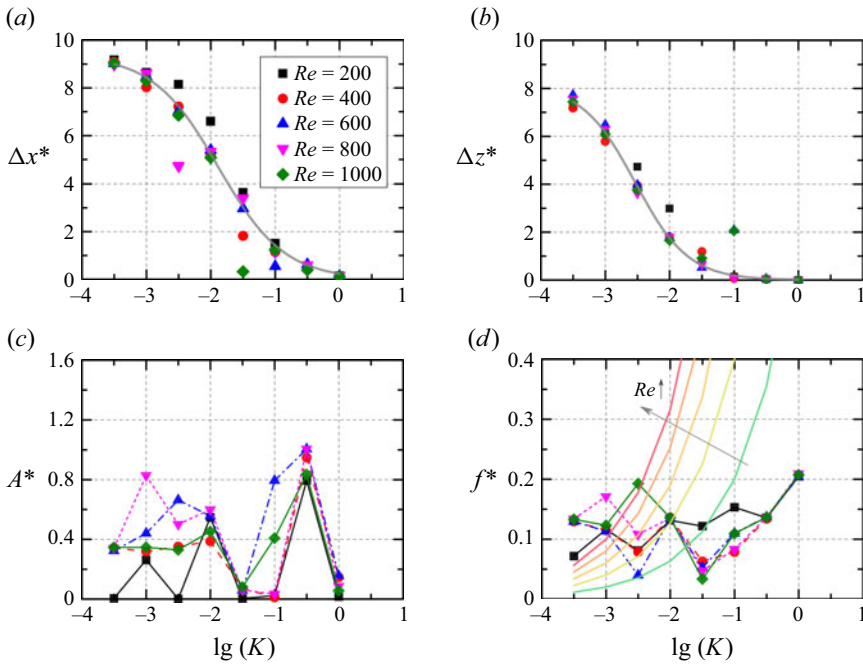


Figure 17. Statistics of the stem response with different stiffness ratios at  $Re = 200$ – $1000$ . (a, b) The mean position shift, (c) the transverse amplitude and (d) dominant frequency of the transverse displacement. The solid lines in (a) and (b) denote the fitted equations and the correlation coefficients ( $R^2$ ) are both 0.997. The solid lines in (d) represent the first natural frequency ( $f_{n,1}$ ) at different  $Re$  values. The arrow indicates the increase of  $Re$  from 200 to 1000.

### 6.1. Characteristics of shape deformation and stem response

The mean position of the stem tip in different directions serves as a crucial indicator of hydrodynamic loading. Figure 17 shows the mean position, vibration amplitude and frequency of the stem tip in different directions. The mean position shifts are defined as  $\Delta x^* = (\bar{x}_t - \bar{x}_{t,0})/D$ ,  $\Delta y^* = (\bar{y}_t - \bar{y}_{t,0})/D$  and  $\Delta z^* = (\bar{l}_t - \bar{l}_{t,0})/D$ , where the subscript 0 denotes initial values. Due to the circular cross-section's rotational symmetry, transverse shifts remain zero in most simulations and are not further discussed. As shown in figure 17(a), for  $Re = 200$ – $1000$ , the streamwise shift ( $\Delta x^*$ ) follows a consistent trend. Excluding divergent cases, the best-fit nonlinear equation is  $\Delta x^* = 9.4/(1 + e^{1.96(\lg(K)+1.88)})$  with a correlation coefficient ( $R^2 > 0.99$ ), see figure 17(a). This suggests that the streamwise deformation is independent of  $Re$ . Similarly, the vertical shift ( $\Delta z^*$ ) follows a similar equation:  $\Delta z^* = 8.1/(1 + e^{2.42(\lg(K)+2.54)})$ , see figure 17(b). Luhar & Nepf (2011) proposed a scaling law for the effective length of the blade under uniform flow. The effective length could be scaled as  $l_e/l \sim K^{1/3}$ . Here, the effective length ( $l_e$ ) is defined as the length of a rigid vertical blade that generates the same drag as the flexible blade of total length ( $l$ ). In the present study, the deflected length ( $l_d$ ) is scaled as  $l_d/l \sim K^{1.05}$ . The exponent is higher than that in Luhar & Nepf (2011). We assume the difference is likely caused by three factors: (i) the stem in the present study is circular cross-sectional, (ii) the consistently higher deflected height compared with effective height (Luhar & Nepf 2011; Luhar 2012) and (iii) for a circular stem, the transverse vibration leads to stronger spanwise vortices, contributing to higher mean drag (Sarpkaya 2004).

Despite significant deformation in streamwise and vertical directions, vibrations in these directions remain negligible. No further discussion on them is presented. The transverse



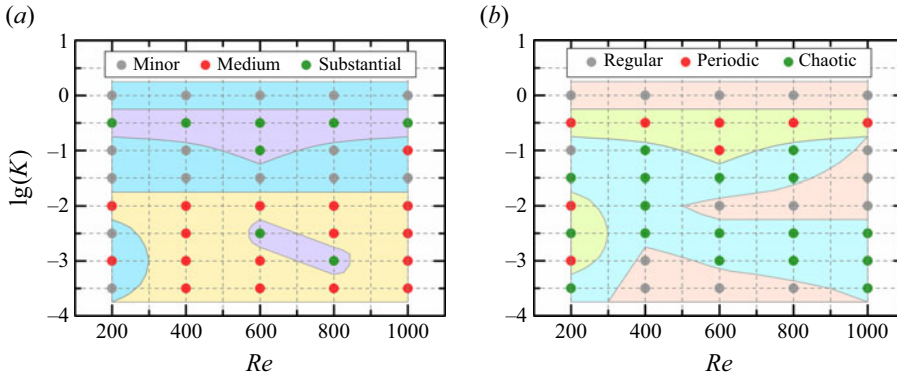


Figure 18. The regimes of the response are defined based on (a) the transverse amplitude and (b) the spectral features of the displacement. Here, the minor vibration is defined as  $A^* < 0.2$ , medium vibration is defined as  $0.2 \leq A^* \leq 0.6$  and substantial vibration is defined as  $A^* > 0.6$ . The phase portrait of the transverse displacement is applied to identify the types.

amplitude is defined as  $A^* = \sqrt{2}y_{rms}/D$ , where  $y_{rms}$  is the r.m.s. transverse displacement. Figure 17(c) shows that the transverse response does not exhibit a clear dependence on  $\lg(K)$ , suggesting that vortex shedding is not persistently locked to the natural frequency. The  $i$ th natural frequency of the flexible stem is given by

$$f_{n,i} = \frac{k_i^2}{2\pi} \sqrt{\frac{EI}{m + m_a}}, \quad (6.1)$$

where  $i$  is the mode number,  $m$  is the structure mass,  $m_a$  is the added mass of the fluid defined as  $m_a = \pi D^2 \rho_f l / 4$  and  $k_i$  is the dimensionless frequency parameter of the  $i$ th mode. The first and second modal parameters are  $k_1 = 1.875$  and  $k_2 = 4.694$  (Blevins 2016). For conciseness, only the first natural frequency (i.e.  $f_{n,1}$ ) is shown in figure 17(d). At specific  $\lg(K)$  values, the dominant frequency aligns with  $f_{n,1}$ , with locking to  $f_{n,2}$  observed at  $Re = 200$  (not shown).

The highest amplitude occurs at  $\lg(K) = -0.5$ . At the lowest  $\lg(K)$ , transverse amplitude is tiny as the stem yields more readily to the incoming flow, exhibiting ‘high flexibility-induced rigidity’ (He, Liu & Shen 2022). The dominant frequency (i.e.  $f^*$ ) of transverse displacement is shown in figure 17(d). At  $Re = 200$ , the dominant frequency grows roughly with  $\lg(K)$ . However, for  $Re = 400$ – $1000$ , dominant frequencies are irregular, mostly clustering around  $f^* = 0.1$ . As discussed in § 5, more complex vortical structures at the higher  $Re$  influence displacement. Unlike an infinite cylinder experiencing VIV, where  $f^* > 0.2$  for  $Re > 200$  (Wang, Xiao & Incecik 2017; Gsell, Bourguet & Braza 2019; Yu *et al.* 2024), vortex shedding in a wall-mounted flexible cylinder is significantly slower due to junction-induced vortex retardation.

Based on transverse amplitude and displacement characteristics, responses are categorised into three types, see figure 18. Based on the amplitude, the three types are minor vibration (i.e.  $A^* < 0.2$ ), medium vibration (i.e.  $0.2 \leq A^* \leq 0.6$ ) and substantial vibration (i.e.  $A^* > 0.6$ ), see figure 18(a). Minor vibration primarily occurs in three regions:  $\lg(K) = 0$ ,  $\lg(K) = -1.0$ – $-1.5$ , and  $\lg(K) = -2.5$ – $-3.5$  (for  $Re = 200$  only). In the first region, the stem is relatively rigid, with small transverse amplitude, and vortex shedding dominates vibration ( $f^* = 0.205$ ), see figure 19(a–i). With the same  $K$  but at a higher  $Re$ , stronger vortex shedding increases the hydrodynamic loads, slightly amplifying the vibration while still remaining in the minor vibration category. In the second region,

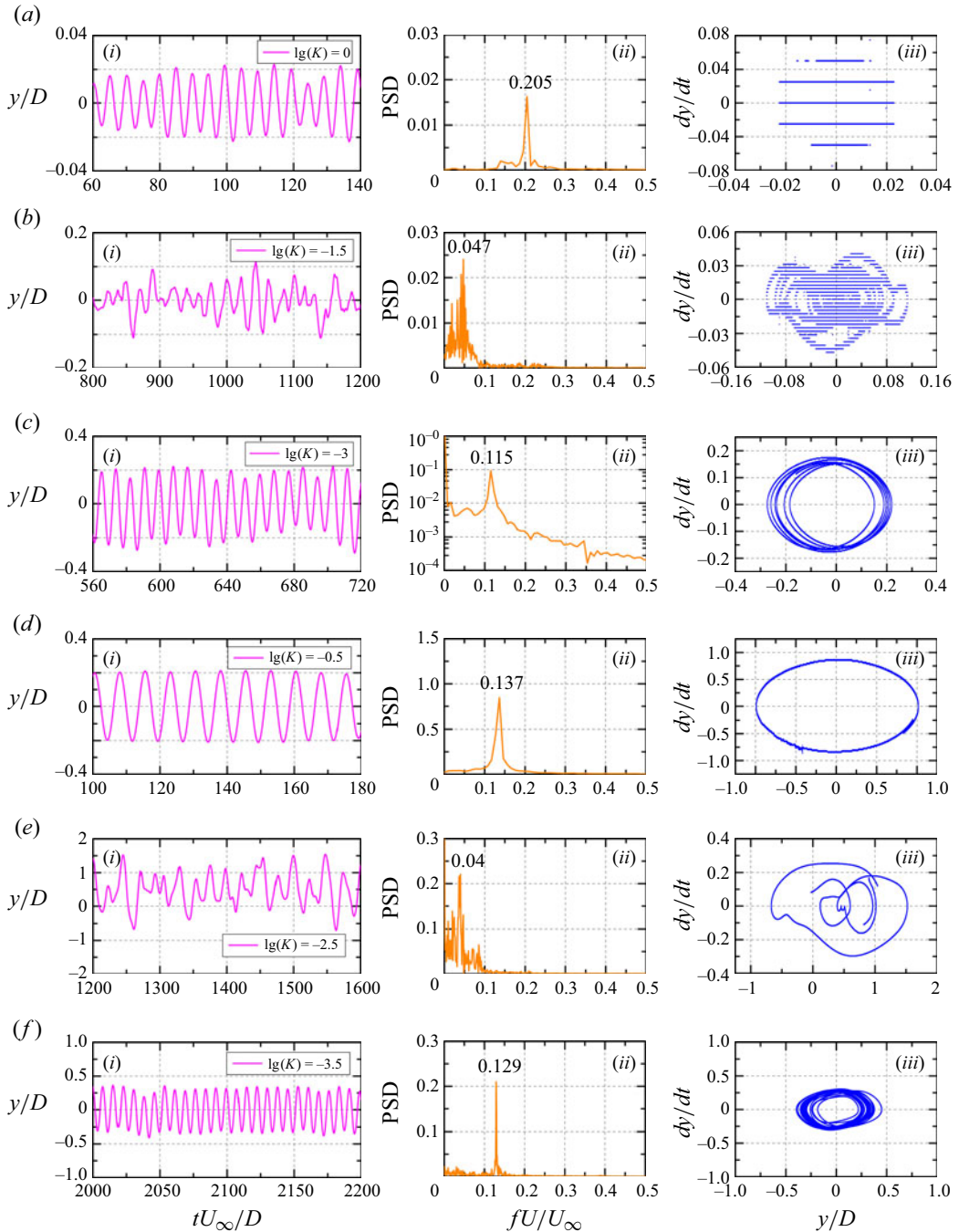


Figure 19. Time histories (left column), power spectral density (middle column) and phase portraits of the transverse displacement (right column) at the stem tip at different  $Re$  and  $\lg(K)$ . Panels show (a)  $Re = 200$  and  $\lg(K) = 0$ , (b)  $Re = 800$  and  $\lg(K) = -1.5$ , (c)  $Re = 400$  and  $\lg(K) = -3.0$ , (d)  $Re = 600$  and  $\lg(K) = -0.5$ , (e)  $Re = 600$  and  $\lg(K) = -2.5$  and (f)  $Re = 600$  and  $\lg(K) = -3.5$ . Note that the discrete points are used in the phase portraits.

the vortex shedding frequency deviates from the stem's first natural frequency. As shown in figure 19(b-i,b-ii), the dominant frequency ( $f^* = 0.047$ ) in this region is much lower and significantly differs from the natural frequency. Unlike the first region, multiple comparable low frequencies are observed, even though the transverse amplitude is higher. The third region occurs at  $\lg(K) < -2.0$  and  $Re = 200$ , where the stem approaches a lodging state, and the vortical structures remain regular, as discussed in § 6.3.

Medium vibration mainly appears at  $\lg(K) \leq -2.0$ , see figure 18(a). As shown in figure 19(c-i), although the transverse amplitude is slightly above  $A^* = 0.2$ , the displacement remains regular. The dominant frequency is  $f^* = 0.115$ , with a magnitude significantly higher than those of other frequency components, see figure 19(c-ii). Due to substantial deformation, the vortex shedding frequency in this case is lower.

Substantial vibration occurs in two regions:  $\lg(K) = -0.5$ – $1.0$  with  $Re = 200$ – $1000$  and  $\lg(K) = -2.0$ – $3.0$  with  $Re = 600$ – $800$ , see figure 18(a). In the first region, the transverse amplitude is larger than in the second region, which may indicate better synchronisation between stem vibration and vortex shedding. In the first region, the displacement is periodic, and the stem vibration is dominated by a single frequency ( $f^* = 0.137$ ), see figure 19(d-i,d-ii). In contrast, in the second region, the displacement is chaotic, and multiple low-frequency components dominate stem vibration, see figure 19(e-i,e-ii). The dominant frequency is  $f^* = 0.04$ , which is significantly lower than the stem's natural frequency.

The phase portrait provides a geometric representation of a dynamical system's trajectories in the phase plane and is used to confirm the system dynamics (Jordan & Smith 2007). In this study, phase portraits of displacement are employed to illustrate the system dynamics (Chang & Modarres-Sadeghi 2014). Based on the characteristics of transverse displacement portraits, the response is classified into three categories, i.e. periodic, regular (quasiperiodic) and chaotic. The distribution of these categories is shown in figure 18(b). The spectral content of the displacement serves as a supplementary indicator. Periodic vibration is characterised by a dominant frequency with a significantly higher magnitude than other frequencies, see figure 19(d-ii,d-iii). Synchronisation between vortex shedding and stem vibration is observed. Comparing figures 18(a) and 18(b), the first periodic region coincides with the first substantial vibration region, suggesting that higher amplitudes facilitate periodic vortex shedding. The second periodic region appears at  $\lg(K) = -2.0$ – $3.0$  but only for  $Re = 200$ . In this region, the transverse amplitude is moderate, and vortex shedding remains periodic. Beyond  $Re = 200$  finer vortices emerge, and low-frequency components appear. A more flexible stem is more susceptible to turbulent fluctuation, making periodic vibration nearly impossible when  $\lg(K) < -1.0$ .

Regular vibration is observed in three regions, see figure 18(b). The first region occurs at  $\lg(K) = 0$  with  $Re = 200$ – $1000$ , where the stem is relatively rigid, and its vibration is regulated by vortex shedding, maintaining a steady rhythm, see figure 19(a-ii). The phase portrait in figure 19(a-iii) indicates that stem vibration follows a nearly constant trajectory. The second region, at  $\lg(K) = -1.0$ – $2.0$  with  $Re = 600$ – $1000$ , exhibits transverse amplitude ranging from minor to substantial. As shown in figure 19(c-ii), the dominant frequency is  $f^* = 0.115$ , while other frequency components are insignificant in magnitude. The phase portrait in figure 19(c-iii) is highly regular. The third region, at  $\lg(K) = -3.0$ – $3.5$  with  $Re = 400$ – $800$ , shows an intermediate stem amplitude with a single frequency,  $f^* = 0.129$ , see figure 19(f-ii).

The chaotic regime spans  $\lg(K) = -1.0$ – $3.5$  and  $Re = 200$ – $1000$ , see figure 18(b). A comparison of figures 18(a) and 18(b) reveals that chaotic vibration can occur regardless of whether the transverse amplitude is small, medium or substantial. At moderate  $\lg(K) (= -1.0$ – $1.5)$ , the transverse amplitude is small, but multiple low frequencies appear, see figure 19(b-i,b-ii). The phase portrait in figure 19(b-iii) further confirms

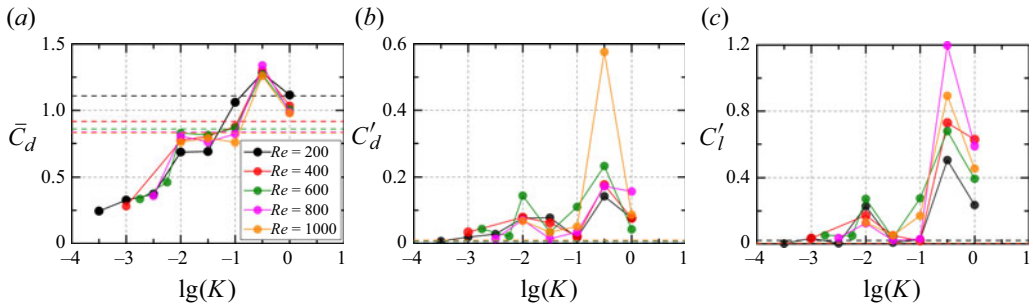


Figure 20. Hydrodynamic forces on a wall-mounted flexible stem with  $\lg(K)$  at  $Re = 200$ –1000. (a) Mean drag ( $\bar{C}_d$ ), (b) r.m.s. drag ( $C'_d$ ) and (c) r.m.s. lift ( $C'_l$ ). In each plot, the horizontal lines (with the same colours as the flexible case) denote the corresponding forces on the rigid stem.

this chaotic behaviour. At lower  $\lg(K)$  ( $= -2.0 - 3.5$ ), the transverse amplitude may be medium or substantial, but stem vibration is strongly influenced by turbulent structures, leading to chaotic behaviour, see figure 19(e-i, e-ii). The dominant frequency ( $f^* = 0.04$ ) is significantly low, with several comparable low-frequency component. The phase portrait in figure 19(e-iii) indicates no fixed trajectory for the stem to follow.

### 6.2. Hydrodynamic forces and comparison with the rigid stem

The hydrodynamic forces on the flexible stem are key factors influencing stem oscillation and shape deformation. Figure 20 shows the variation of hydrodynamic forces on the flexible stem as a function of  $Re$  and  $\lg(K)$ . For comparison, results of a rigid stem are superimposed. As shown in figure 20(a), the mean drag coefficient ( $\bar{C}_d$ ) generally decreases as  $\lg(K)$  decreases, indicating that  $\bar{C}_d$  is primarily affected by stem deformation. As mentioned in § 6.1, when stiffness is significantly low, the deflected height of the stem decreases, resulting in a more streamlined shape and a corresponding reduction in  $\bar{C}_d$  drops. For the two cases with the highest stiffnesses, i.e.  $\lg(K) = 0$  and  $-0.5$ , the  $\bar{C}_d$  of the flexible stem is higher than that of the rigid stem. In these cases, shape deformation is minimal, but stem oscillation develops, particularly for  $\lg(K) = -0.5$ . This suggests that transverse oscillation has a significant impact on  $\bar{C}_d$  when the stem is relatively rigid.

The r.m.s. drag and lift coefficients vary significantly with  $\lg(K)$ . As shown in figure 20(b), the r.m.s. drag coefficient ( $C'_d$ ) increases gradually with increasing  $\lg(K)$ . However, it is slightly lower for the cases with  $\lg(K) = 0$  and  $-1$  due to weak transverse oscillation. For a flexible stem with identical deformation, stronger transverse oscillation enhances vortex shedding, leading to higher  $C'_d$ . As shown in figure 20(c), in most cases, the r.m.s. lift coefficient ( $C'_l$ ) on the flexible stem is comparable to that of the rigid stem. However, it is significantly higher for  $\lg(K) = 0, -0.5$  and  $-2.0$ , where transverse amplitude is larger. This suggests that  $C'_l$  is strongly influenced by transverse oscillation.

### 6.3. Characteristics of the 3-D vortical structures at different regimes

The 3-D vortical structures provide valuable insights into the physics of different responses and hydrodynamic loads acting on the flexible stem. Figure 21 shows the detailed 3-D vortical structures at  $Re = 200$  with  $\lg(K) = 0 - 3.5$ . The vortex dynamics of the flexible stem, including vortex arrangement and shedding behaviour, differs significantly from the rigid case. At the highest  $\lg(K)$ , the stem experiences minimal deformation and behaves similarly to a rigid stem (Luhar & Nepf 2011, 2016; Jacobsen *et al.* 2019). As shown in figure 21(a), at  $\lg(K) = 0$ , the wake resembles that of a rigid stem, although some

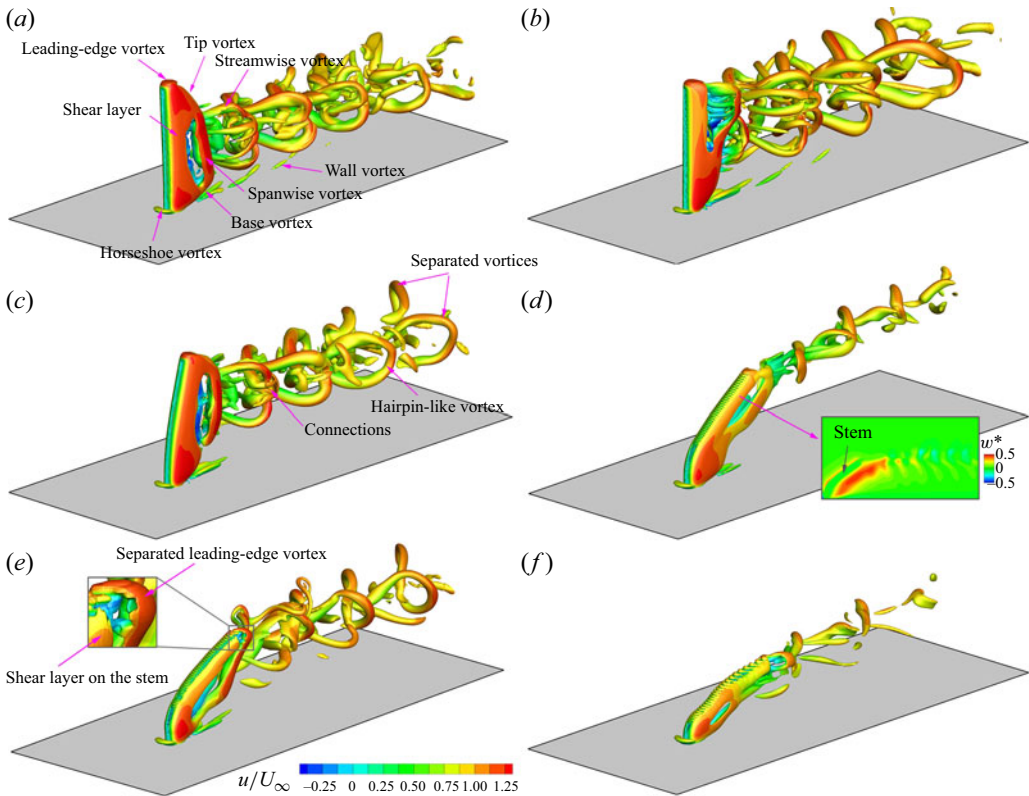


Figure 21. The 3-D vortical structures of a wall-mounted flexible stem at  $Re = 200$  and different  $K$  values. Panels show (a)  $\lg(K) = 0$ , (b)  $\lg(K) = -0.5$ , (c)  $\lg(K) = -1.0$ , (d)  $\lg(K) = -1.5$ , (e)  $\lg(K) = -2.0$  and (f)  $\lg(K) = -3.0$ . Flow is from left to right. Here,  $Q = 5$ . The plot in (b) is the corresponding vertical velocity field at the midplane of the  $y$ -direction.

alterations occur due to stem vibration. The spanwise vortex shedding occurs at an angle of approximately  $6^\circ$  relative to the wall surface, which is considerably lower than the  $\approx 21^\circ$  observed in the rigid case. The downwash flow in the flexible case has a weaker effect on vortex formation, and similar to the rigid case, the spanwise vortices mainly appear around the midspan. At  $\lg(K) = -0.5$ , the stem oscillates with a large transverse amplitude ( $A^* = 0.79$ ), leading to significant changes in vortical structures. The shift in vortex shedding is associated with the increased transverse amplitude, which enhances vortex formation near the tip despite minor deformation. Consequently, the downwash flow effect becomes negligible. As shown in figure 21(b), vortex shedding initiates at the free end and weakens closer to the wall, ceasing at approximately  $2.8D$  from the wall.

As  $\lg(K)$  decreases further, stem deformation becomes pronounced, altering the 3-D vortex distribution. As shown in figure 21(c), deformation leads to a more evenly distributed flow along the stem length. Near the free end, vortex shedding remains approximately parallel, but further downstream, the separated vortices stretch into hairpin-vortex like structures (Robinson 1991). Additionally, vortices from both sides of the stem initially connect during the formation, as marked in figure 21(c), although these connections disappear downstream due to increased vortex head velocity. In the far wake, the vortices are fully hairpin-vortex like.

At  $\lg(K) \leq -1.5$ , significant stem deformation results in spanwise vortex shedding along the entire stem length, although this is weaker than in less deformed cases,



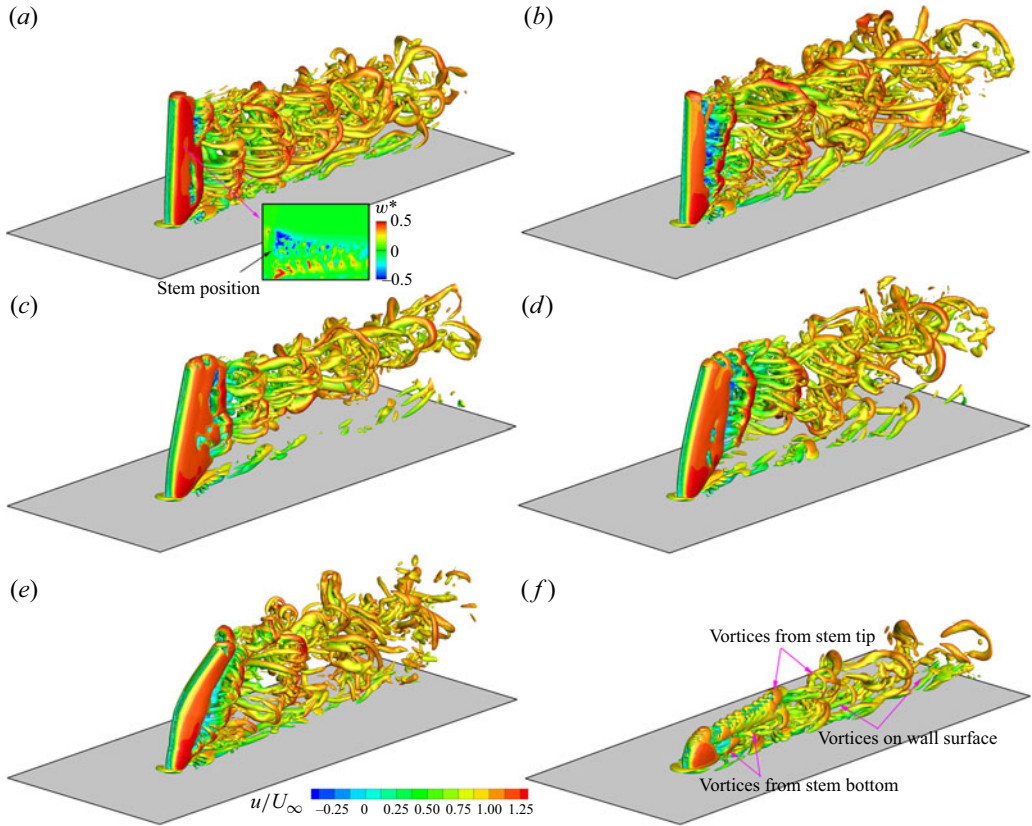


Figure 22. The 3-D vortical structures of a wall-mounted flexible stem at  $Re = 400$  and different  $K$  values. Panels show (a)  $\lg(K) = 0$ , (b)  $\lg(K) = -0.5$ , (c)  $\lg(K) = -1.0$ , (d)  $\lg(K) = -1.5$ , (e)  $\lg(K) = -2.0$  and (f)  $\lg(K) = -3.0$ . Flow is from left to right. Here,  $Q = 20$ . The inset in (a) is the corresponding vertical velocity field at the midplane of the  $y$ -direction.

see figure 21(d–f). As  $\lg(K)$  drops, vortices form progressively closer to the free end. At  $\lg(K) = -1.5$  and  $-3.0$ , transverse amplitudes are smaller, and vortical structures are weaker compared with  $\lg(K) = -2.0$ , where the transverse amplitude is higher ( $A^* = 0.55$ ). Comparing figures 21(d) and 21(e), despite a slightly stronger stem oscillation at  $\lg(K) = -3.0$  than at  $\lg(K) = -1.5$ , the vortical structures at  $\lg(K) = -3.0$  are weaker due to greater deformation. A common feature across these cases is the slow upward movement of vortices, see the inset in figure 21(d). For significantly deformed stems, separation of the attached shear layer at the free-end surface occurs, forming a leading-edge vortex and/or free-end arch vortex (observed in high  $Re$  flow, e.g.  $Re \gtrsim 4 \times 10^3$ , see figure 1). As shown in the inset of figure 21(e), the reattached shear layer at the free-end surface separates, alternately aligned with the vortex shedding. This behaviour is absent in the rigid case. Large deformation makes the attached shear layer more prone to detachment.

Figure 22 shows the organisation of 3-D vortical structures at  $Re = 400$ . As in the rigid case, vortices behind the flexible stem at  $Re = 400$  are stronger than at  $Re = 200$ . As  $\lg(K)$  decreases, stem deformation intensifies, altering the vortical structures. At  $\lg(K) = 0$ , deformation is negligible, and vortex shedding remains similar to the rigid case, see figures 13(b) and 22(a). The downwash flow near the free end impacts a shorter span in the flexible case. As shown in figure 22(a), vortex shedding remains approximately parallel but occurs in two phases, potentially influenced by free-end downwash flow and



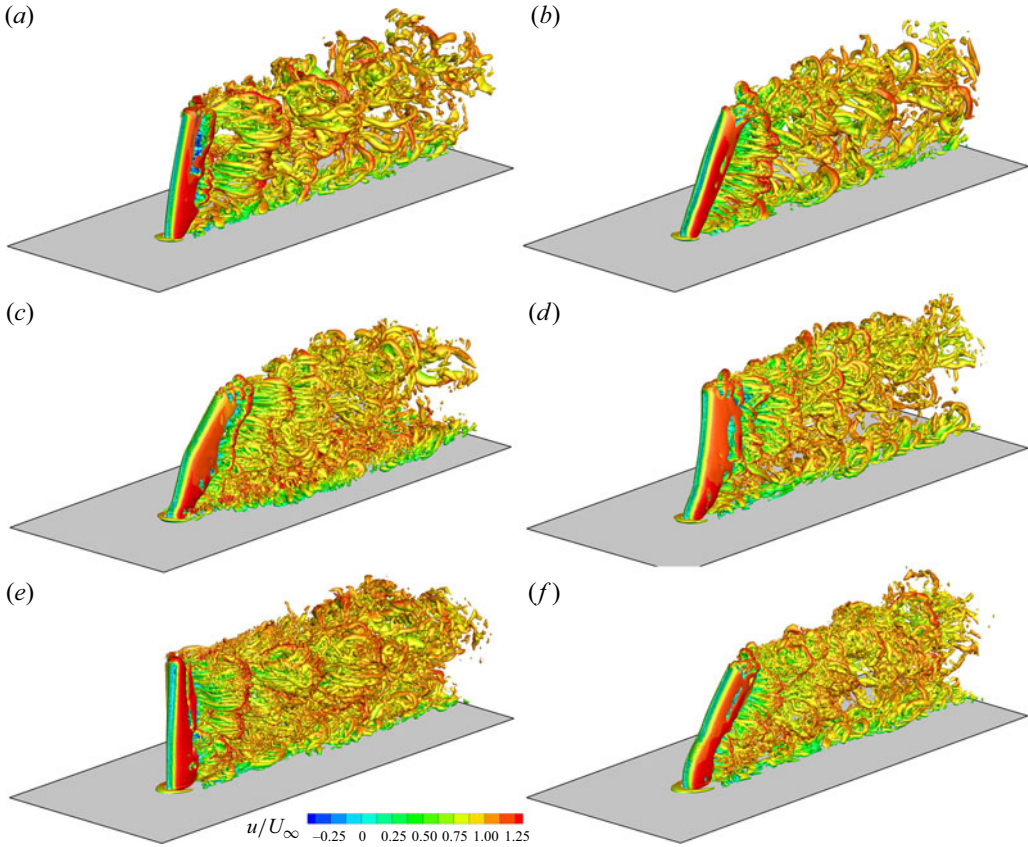


Figure 23. The 3-D vortical structures of a wall-mounted flexible stem at  $Re = 600 - 1000$  and  $K$  values. Panels show (a)  $Re = 600$  and  $\lg(K) = -0.5$ , (b)  $Re = 600$  and  $\lg(K) = -2.0$ , (c)  $Re = 800$  and  $\lg(K) = -1.5$ , (d)  $Re = 800$  and  $\lg(K) = -2.0$ , (e)  $Re = 1000$  and  $\lg(K) = -0.5$ , and (f)  $Re = 1000$  and  $\lg(K) = -2.0$ . Flow is from left to right. Here,  $Q = 45, 80$  and  $125$  for the cases at  $Re = 600, 800$  and  $1000$ , respectively.

junction upwash flow. At  $\lg(K) = -0.5$ , vortex shedding changes drastically, as in the case of  $Re = 200$ . Shedding occurs near the free end, with spanwise vortices forming earlier than those closer to the wall, see figure 22(b). In the near wake, spanwise vortices undergo considerable stretching and slowly move toward the wall. The hairpin vortex on the wall develops and directly interacts with the lower-side vortices from the stem. At  $\lg(K) = -0.5$ , stem oscillation is stronger, and vortex strength is higher than at  $\lg(K) = 0$ .

For lower  $\lg(K)$ , deformation increase significantly. As shown in figure 22(c–f), the vortex dynamics is considerably different as the stem tip nears the wall. Similar to  $Re = 200$ , vortex shedding shifts toward the free end as deformation increases, with vortex intensity generally weakening. However, transverse oscillation impacts both formation position and vortex strength. At  $\lg(K) = -2.0$ , transverse amplitude is larger than at  $\lg(K) = -1.0$  and  $-1.5$ , leading to stronger vortices, see figure 22(c,d,e). At  $\lg(K) = -3.0$ , the stem is nearly lodged against the wall, producing a distinct vortex dynamics, see figure 22(f). Here, spanwise vortices shed only from the stem base and free end. In the near wake, vortices from these positions interact.

Figure 23 shows the arrangement of 3-D vortical structures at  $Re = 600 - 1000$ . At these higher  $Re$ , vortex shedding occurs along nearly the entire stem length, forming

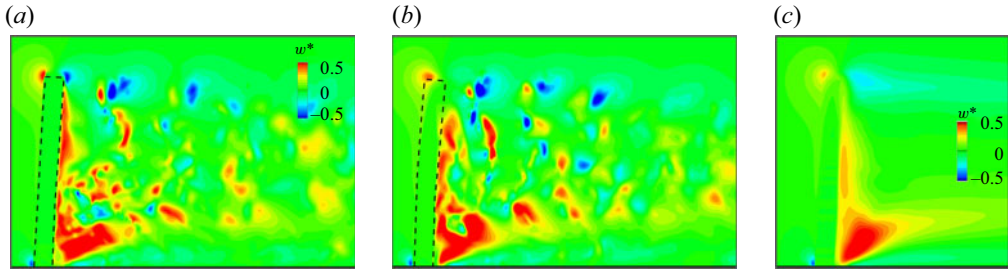


Figure 24. The non-dimensional vertical velocity ( $w^*$ ) of a wall-mounted flexible stem at  $Re = 400$  and  $\lg(K) = -0.5$ . (a,b) instantaneous flow field and (c) time-averaged flow field. The stem position in (a,b) is roughly denoted by the solid lines.

finer vortices. Due to increased instability from lower-part vortices, the wall-developing hairpin vortex strengthens compared with lower  $Re$  ( $= 200\text{--}400$ ) cases. As shown in figure 23(a,b), at  $Re = 600$ , vortex shedding extends from top to bottom but is suppressed at the junction due to the presence of a HV. At  $Re = 800$ , vortex strength increases further, see figure 23(c,d). At  $\lg(K) = -1.5$ , upper-part vortex shedding aligns closely with the deformed stem, while lower-part vortex shedding occurs but dissipates quickly, see figure 23(c). Compared with  $\lg(K) = -1.5$ , transverse oscillation at  $\lg(K) = -2.0$  is stronger, significantly influencing vortex shedding. As shown in figure 23(d), upper-part vortex shedding remains nearly parallel, but lower-part vortex shedding is not synchronised, leading to vortices gradually shifting upward downstream. Consequently, interactions between hairpin and spanwise vortices weaken. The stem exhibits a low-frequency back-and-forth motion, resembling a slow wave, as indicated in figure 23(d). At  $Re = 1000$ , vortex strength intensifies further. At high  $\lg(K)$ , vortex shedding near the tip experiences minor influence from downwash flow, see figure 23(e). The upper and lower parts of the stem shed vortices at different frequencies. In the near wake, separated vortices are significantly stretched and finer than those at the lower  $Re$ . As  $\lg(K) = -2.0$ , stem deformation is pronounced, with upper-part vortex shedding nearly parallel, see figure 23(f). Lower-part vortices interact with the hairpin vortex but dissipate quickly downstream.

## 7. Discussion

In this section, we discuss particular flow dynamics and the stem response in the flexible case, such as significantly weakened downwash flow and physics of low-frequency oscillation in the streamwise and vertical directions.

### 7.1. Significantly weakened downwash flow

As discussed in § 6.3, stem oscillation and shape deformation can significantly modify the vortex dynamics. In this section, we concentrate on the significantly weakened downwash flow through the case of  $Re = 400$  and  $\lg(K) = -0.5$ . In the rigid case, the flow through the free end moves downward, as shown in figures 13(b) and 16(b). Due to the downwash flow, spanwise vortex shedding occurs in the lower part of the stem. Near the junction, the downwash flow also appears. However, in the flexible case, the vortex dynamics differs significantly. As shown in figure 22(b), spanwise vortex shedding appears in the upper part of the stem, with a leading phase closer to the stem tip. The vortex strength also increases due to the larger oscillation amplitude near the tip. Figure 24 shows the vertical velocity field around and behind the stem at  $Re = 400$  and  $\lg(K) = -0.5$ .

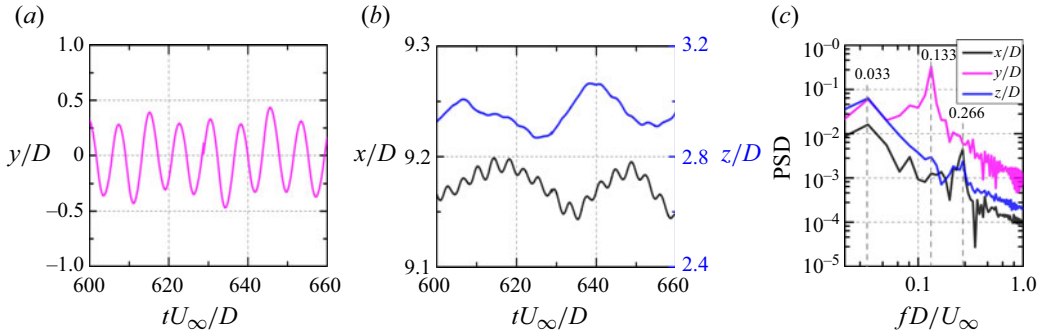


Figure 25. Time histories of the displacement of stem tip at the streamwise, transverse, and spanwise directions for  $Re = 400$  and  $\lg(K) = -3.5$ . (a) for the displacement in the transverse direction and (b) for the displacements in the streamwise and spanwise directions. (c) The PSD of the displacements in the three directions.

The vertical velocity along the stem base remains almost entirely positive, indicating that the flow moves upward starting from the junction. This contrasts with the rigid case, where no upwash flow occurs at the same position, see figures 16(b) and 24(a,b). As shown in figures 16(b) and 24(c), the downwash flow near the free end is much weaker compared with the rigid case, suggesting that downwash flow in the flexible case is greatly reduced.

To further illustrate the development of positive transverse velocity, we analyse the streamlines of the instantaneous flow field corresponding to figure 24(a,b) (not shown here for brevity). We see that the arriving flow near the wall surface goes downstream through both sides of the stem. However, due to the emergence of the near-wake base vortex at the stem base, the flow gradually moves upward along the stem bottom. In the near wake, upwash flow partially appears above the growing hairpin vortices on the wall surface, see figure 24(a,b), significantly promoting the upward motion of lower-part vortices shed from the stem sidewalls. In the far wake, this upward motion slows down. The variations in oscillation amplitude at different vertical positions also play a crucial role. The stem oscillation is expected to be stronger near the free end, causing spanwise vortices to shed earlier, thereby enhancing the upward flow dynamics. On the other hand, as the spanwise vortices form closer to the stem bottom, the recirculation region narrows, reducing the amount of upward-moving flow, as indicated by figure 24(c). In the time-averaged flow field, spanwise vortices at the free end shed alternately and subsequently move downward. as a result, only a very weak downwash flow is observed near the free end, significantly weaker than in the rigid case.

## 7.2. Low-frequency oscillation in the streamwise and vertical directions

A unique low-frequency oscillation phenomenon is observed in the present study. As shown in figure 25(a,c), transverse oscillation is relatively strong, with a dominant frequency of  $f^* = 0.133$ . However, oscillations in the streamwise and vertical directions are much weaker and dominated by a significantly low frequency of  $f^* = 0.033$ , see figure 25(b,c). This suggests that the oscillations in these two directions are governed by flow structures with a very low frequency. In the transverse direction, a secondary frequency of  $f^* = 0.266$  is observed, which corresponds to the second harmonic of the dominant frequency. This is an intrinsic feature of VIV of a circular cylinder (Sarpkaya 2004). The secondary frequency in the streamwise and vertical directions also matches this second harmonic frequency, see figure 25(c). Furthermore, the low-frequency displacement in the vertical direction has a greater magnitude than in the streamwise

direction, indicating that the associated vortical structures have a higher impact in the vertical direction.

As indicated by [figure 17\(a–c\)](#), when the stiffness is notably lower, i.e.  $\lg(K) \leq -3.0$ , the deflected height ( $l_d$ ) of the stem is very small, and the stem aligns almost parallel to the wall. Unsurprisingly, vortex development and subsequent interactions at  $\lg(K) = -3.0$  and  $-3.5$  are similar. Because of significant shape deformation, vortex shedding from the stem can be classified into two regimes, similar to the condition shown in [figure 22\(f\)](#). Near the stem base (i.e. the lower part), spanwise vortex shedding appears, with separated vortices travelling downstream. At the formation position, these vortices have negligible influences on displacement at the stem tip in the streamwise and vertical directions. Meanwhile, the upper part of the stem undergoes significant deformation, becoming nearly parallel to the wall. The incoming flow moves smoothly along the stem length, and the vortex shedding dynamics contrasts with that at the base. Vortex shedding at the stem tip occurs at a high frequency ( $f^* \approx 0.13$ , estimated based on the average velocity and streamwise distance between consecutive vortices) and primarily drives transverse oscillation. Interactions between lower-part vortices and shear layers from the upper part are also witnessed. As vortices from the lower part expand, shear layer development around the upper part, particularly near the lower side, is significantly influenced. Near the stem tip, these interactions reach their strongest, affecting the local pressure distribution. This interaction is responsible for the low-frequency components of displacement in the streamwise and vertical directions.

## 8. Conclusions

In this study, we simulated the wall-mounted stem in uniform flow using a newly coupled method – the IBM–VFIFE method. The 3-D flow characteristics and stem dynamics were analysed in detail. In the rigid case, we identified three flow regimes based on force spectra and the vortex dynamics. The first regime (R1, at  $Re = 200$ ) features periodic hydrodynamic forces and a single vortex shedding frequency. The second regime (R2, at  $Re = 400$ ) is characterised by higher forces and two vortex shedding frequencies, one of which is significantly lower than the other. The third regime (R3, at  $Re = 600$ – $1000$ ) is dominated by one low frequency. Distinctive 3-D vortex structures were observed in these regimes. In R1, the vortex structures are regular but slant-arranged in the near wake. In R2, the vortex structures become irregular while take over a longer length. In R3, vortex sheddings at different vertical positions are nearly synchronised. As  $Re$  increases, the streamwise vortices become finer in scale.

The dynamics of a flexible stem at  $Re = 200$ – $1000$  was thoroughly explored. It demonstrated that stem oscillation and shape deformation are closely correlated with stiffness ( $K$ ). Transverse oscillation is much stronger than oscillation in the other two directions, playing a more prominent role in vortex shedding. Within the studied  $Re$ , the highest amplitude is observed at  $\lg(K) = -0.5$ . Stem deformation is well approximated by a nonlinear equation. The deflected length is scaled as  $l_d/l \sim K^{1.05}$ , with a higher exponent compared with that reported for a blade in Luhar & Nepf (2011), likely due to differences in cross-section, greater deflected height and stronger spanwise vortex shedding. Hydrodynamic forces are influenced by both stem oscillation and shape deformation: oscillation dominates at high  $K$ , while deformation has a stronger effect at low  $K$ .

We identified three oscillation regimes in terms of the transverse amplitude: minor vibration for  $A^* < 0.2$ , medium vibration for  $0.2 \leq A^* \leq 0.6$  and substantial vibration for  $A^* > 0.6$ . Minor vibration occurs when the stem is either highly rigid or highly

flexible, or when there is a frequency mismatch between vortex shedding and stem's natural frequency. Medium vibration is mostly observed at  $\lg(K) \leq -2.0$ . Substantial vibration occurs in two regions: one at  $\lg(K) = -0.5$ – $-1.0$  for  $Re = 600$ – $800$  and the other at  $\lg(K) = -2.0$ – $-3.0$  for all studied  $Re$ . In terms of transverse displacement characteristics, the response can be classified into three regimes: regular, periodic and chaotic regimes. Periodic vibration is observed in two regions: one corresponding to the first substantial vibration region and the other at  $\lg(K) = -2.0$ – $-3.0$  but only  $Re = 200$ . The regular regime is assigned to three parts: the first at  $\lg(K) = 0$  within the studied  $Re$ , the second at  $\lg(K) = -1.0$ – $-2.0$  and  $Re = 600$ – $1000$ , and the third at  $\lg(K) = -3.0$ – $-3.5$  and  $Re = 400$ – $800$ . Chaotic vibration spans  $\lg(K) = -1.0$ – $-3.5$  within the simulated  $Re$ , regardless of the amplitude. We revealed the influences of stem oscillation and shape deformation on hydrodynamic forces acting on the flexible stem. It is found that the flexible stem experiences higher drag under relatively rigid conditions compared with a fully rigid stem.

We found that both the stem oscillation and shape deformation are crucial in determining vortex dynamics around the stem. Oscillation enhances vortex strength and alters vortex distribution, while shape deformation significantly modifies the flow field, such as by generating strong upwash flow from the junction. Compared with the rigid case, downwash flow in the flexible case has a weaker effect on vortex formation. We confirmed distinctive physical behaviours of flexible stems, depending on  $Re$  and  $\lg(K)$ . Downwash flow is notably weakened or absent due to strong deformation, which induces upwash flow. Low-frequency oscillation occurs in the streamwise and vertical directions, suggesting that different flow structures govern oscillations in these two directions.

The numerical method provided in this study has clear advantages for simulating wall-mounted structures under different flow conditions. It shows great potential for engineering applications and theoretical advancements, such as understanding how the total drag of a circular or rectangular patch of vegetation/stems is affected by stem flexibility (Koken & Constantinescu 2021, 2023).

**Acknowledgements.** We thank Professor C. Ji from Tianjin University, Professor D. Xu from Hohai University, Mr Y. Wu and J. Ni from Tianjin University for their contributions to the IBM–VFIFE method. We thank anonymous referees for their constructive suggestions and comments, which help a lot in improving the quality of this paper. This work was supported with computational resources provided by the National Supercomputing Centre, Singapore (<https://www.nscg.sg>), under project ID: 11002459 and 11003759.

**Funding.** This project is funded by the Research, Innovation and Enterprise 2025 Coastal Protection and Flood Management Research Programme. The authors are grateful to the National Research Foundation of Singapore, PUB (Singapore's National Water Agency) for supporting this work done in the Coastal Protection and Flood Resilience Institute (CFI) Singapore under the project grant H1-P3.

**Declaration of interests.** The authors report no conflict of interest.

## REFERENCES

- ADARAMOLA, M.S., AKINLADE, O.G., SUMNER, D., BERGSTROM, D.J. & SCHENSTEAD, A.J. 2006 Turbulent wake of a finite circular cylinder of small aspect ratio. *J. Fluids Struct.* **22** (6), 919–928.
- BABAN, F., SO, R.M.C. & OTUGEN, M.V. 1989 Unsteady forces on circular cylinders in a crossflow. *Exp. Fluids* **7**, 293–302.
- BAKER, C.J. 1979 The laminar horseshoe vortex. *J. Fluid Mech.* **95** (2), 347–367.
- BLEVINS, R.D. 2016 *Formulas for Dynamics, Acoustics and Vibration*. Wiley.
- BOURGEOIS, J.A., SATTARI, P. & MARTINUZZI, R.J. 2011 Alternating half-loop shedding in the turbulent wake of a finite surface-mounted square cylinder with a thin boundary layer. *Phys. Fluids* **23** (9), 095101.
- BOURGEOIS, J.A., SATTARI, P. & MARTINUZZI, R.J. 2012 Coherent vortical and straining structures in the finite wall-mounted square cylinder wake. *Intl J. Heat Fluid Flow* **35**, 130–140.



- BRADLEY, K. & HOUSER, C. 2009 Relative velocity of seagrass blades: implications for wave attenuation in low-energy environments. *J. Geophys. Res.* **114** (F1), F01004.
- CAO, Y., TAMURA, T., ZHOU, D., BAO, Y. & HAN, Z. 2022 Topological description of near-wall flows around a surface-mounted square cylinder at high Reynolds numbers. *J. Fluid Mech.* **933**, A39.
- CHANG, G.H. & MODARRES-SADEGHI, Y. 2014 Flow-induced oscillations of a cantilevered pipe conveying fluid with base excitation. *J. Sound Vib.* **333** (18), 4265–4280.
- CHANG, W.Y., CONSTANTINESCU, G. & TSAI, W.F. 2017 On the flow and coherent structures generated by an array of rigid emerged cylinders placed in an open channel with flat and deformed bed. *J. Fluid Mech.* **831**, 1–40.
- CHANG, W.Y., CONSTANTINESCU, G. & TSAI, W.F. 2020 Effect of array submergence on flow and coherent structures through and around a circular array of rigid vertical cylinders. *Phys. Fluids* **32** (3), 035110.
- CHEN, W., JI, C., ALAM, M.M. & YAN, Y. 2022 Three-dimensional flow past two stationary side-by-side circular cylinders. *Ocean Engng* **244**, 110379.
- DEARDORFF, J.W. 1970 A numerical study of three-dimensional turbulent channel flow at large Reynolds numbers. *J. Fluid Mech.* **41** (2), 453–480.
- DERAKHSHANDEH, J.F. & ALAM, M.M. 2019 A review of bluff body wakes. *Ocean Engng* **182**, 475–488.
- DUAN, Y.F., HE, K., ZHANG, H.M., TING, E.C., WANG, C.Y., CHEN, S.K. & WANG, R.Z. 2014 Entire-process simulation of earthquake-induced collapse of a mockup cable-stayed bridge by vector form intrinsic finite element (VFI) method. *Adv. Struct. Engng* **17** (3), 347–360.
- ESSEL, E.E., TACHIE, M.F. & BALACHANDAR, R. 2021 Time-resolved wake dynamics of finite wall-mounted circular cylinders submerged in a turbulent boundary layer. *J. Fluid Mech.* **917**, A8.
- ETZOLD, F. & FIEDLER, H. 1976 The near-wake structure of a cantilevered cylinder in a cross-flow. *Z. Flugwiss.* **24**, 77–82.
- FINNIGAN, J. 2000 Turbulence in plant canopies. *Annu. Rev. Fluid Mech.* **32** (1), 519–571.
- FREDERICH, O., WASSEN, E. & THIELE, F. 2008 Prediction of the flow around a short wall-mounted finite cylinder using LES and DES. *J. Numer. Anal. Ind. Appl. Maths* **3** (3-4), 231–247.
- FRÖHLICH, J. & RODI, W. 2004 LES of the flow around a circular cylinder of finite height. *Int. J. Heat Fluid Flow* **25**, 537–548.
- GAYLORD, B. & DENNY, M. 1997 Flow and flexibility. I. Effects of size, shape and stiffness in determining wave forces on the stipitate kelps *Eisenia arborea* and *Pterygophora californica*. *J. Exp. Biol.* **200** (24), 3141–3164.
- GHISALBERTI, M. 2000 Mixing Layers and Coherent Structures in Vegetated Aquatic Flows. *M.S. thesis*, Massachusetts Institute of Technology, USA.
- GHISALBERTI, M. & NEPF, H.M. 2002 Mixing layer and coherent structures in vegetated aquatic flows. *J. Geophys. Res.* **107** (C2), 3-1–3-11.
- GRECO, J.J. 1990 The flow structure in the vicinity of a cylinder-flat plate juncture: flow regimes, periodicity and vortex interactions. *M.S. thesis*, Lehigh University, USA.
- GSELL, S., BOURGUET, R. & BRAZA, M. 2019 One- versus two-degree-of-freedom vortex-induced vibrations of a circular cylinder at  $Re = 3900$ . *J. Fluids Struct.* **85**, 165–180.
- HAIN, R., KAHLER, C.J. & MICHAELIS, D. 2008 Tomographic and time resolved PIV measurements on a finite cylinder mounted on a flat plate. *Exp. Fluids* **45** (4), 715–724.
- HAJIMIRZAE, S.M., WOJCIK, C.J. & BUCHHOLZ, J.H.J. 2012 The role of shape and relative submergence on the structure of wakes of low-aspect-ratio wall-mounted bodies. *Exp. Fluids* **53** (6), 1943–1962.
- HE, G.-S., WANG, J.-J., PAN, C., FENG, L.-H., GAO, Q. & RINOSHIKA, A. 2017 Vortex dynamics for flow over a circular cylinder in proximity to a wall. *J. Fluid Mech.* **12**, 698–720.
- HE, S., LIU, H. & SHEN, L. 2022 Simulation-based study of turbulent aquatic canopy flows with flexible stems. *J. Fluid Mech.* **947**, A33.
- HEARST, R.J., GOMIT, G. & GANAPATHISUBRAMANI, B. 2016 Effect of turbulence on the wake of a wall-mounted cube. *J. Fluid Mech.* **804**, 513–530.
- HOSSEINI, Z., BOURGEOIS, J.A. & MARTINUZZI, R.J. 2013 Large-scale structures in dipole and quadrupole wakes of a wall-mounted finite rectangular cylinder. *Exp. Fluids* **54** (9), 1595.
- HOU, X., FANG, Z. & ZHANG, X. 2018 Static contact analysis of spiral bevel gear based on modified VFI (vector form intrinsic finite element) method. *Appl. Math. Model.* **60**, 192–207.
- HU, J., MEI, C.C., CHANG, C.-W. & LIU, P.L.-F. 2021 Effect of flexible coastal vegetation on waves in water of intermediate depth. *Coast. Engng* **168**, 103937.
- HU, Z., HUANG, L. & LI, Y. 2023 Fully-coupled hydroelastic modeling of a deformable wall in waves. *Coast. Engng* **179**, 104245.
- HU, Z. & LI, Y. 2023 Two-dimensional simulations of large-scale violent breaking wave impacts on a flexible wall. *Coast. Engng* **185**, 104370.

- HUANG, W.-X., SHIN, S.J. & SUNG, H.J. 2007 Simulation of flexible filaments in a uniform flow by the immersed boundary method. *J. Comput. Phys.* **226** (2), 2206–2228.
- HUNT, J.C.R., ABELL, C.J.J., PETERKA, A. & WOO, H. 1978 Kinematical studies of the flows around free or surface-mounted obstacles: applying topology to flow visualization. *J. Fluid Mech.* **86** (1), 179–200.
- HUSSEIN, H.J. & MARTINUZZI, R.J. 1996 Energy balance of turbulent flow around a surface mounted cube placed in a channel. *Phys. Fluids* **8** (3), 764–780.
- HWANG, J.Y. & YANG, K.S. 2004 Numerical study of vortical structures around a wall-mounted cubic obstacle in channel flow. *Phys. Fluids* **16** (7), 2382–2394.
- JACOBSEN, N.G., BAKKER, W., UJTTEWAAL, W.S.J. & UITTENBOGAARD, R. 2019 Experimental investigation of the wave-induced motion of and force distribution along a flexible stem. *J. Fluid Mech.* **880**, 1036–1069.
- Ji, C., MUNJIZA, A. & WILLIAMS, J.J.R. 2012 A novel iterative direct-forcing immersed boundary method and its finite volume applications. *J. Comput. Phys.* **231** (4), 1797–1821.
- JIANG, H., CHENG, L., DRAPER, S., AN, H. & TONG, F. 2016 Three-dimensional direct numerical simulation of wake transitions of a circular cylinder. *J. Fluid Mech.* **801**, 353–391.
- JIN, Y.Q., KIM, J.T., FU, S. & CHAMORRO, L.P. 2019 Flow-induced motions of flexible plates: fluttering, twisting and orbital modes. *J. Fluid Mech.* **864**, 273–285.
- JIN, Y.Q., KIM, J.T., MAO, Z. & CHAMORRO, L.P. 2018 On the couple dynamics of wall-mounted flexible plates in tandem. *J. Fluid Mech.* **852**, R2.
- JORDAN, D.W. & SMITH, P. 2007 *Nonlinear Ordinary Differential Equations: an Introduction for Scientists and Engineers*. 4th edn. Oxford University Press.
- KAWAMURA, T., HIWADA, M., HIBINO, T., MABUCHI, I. & KUMADA, M. 1984 Flow around a finite circular cylinder on a flat plate: cylinder height greater than turbulent boundary layer thickness. *Bull. JSME* **27** (232), 2142–2151.
- KIRKIL, G. & CONSTANTINESCU, G. 2012 A numerical study of the laminar necklace vortex system and its effect on the wake for a circular cylinder. *Phys. Fluids* **24** (7), 073602.
- KOKEN, M. & CONSTANTINESCU, G. 2021 Flow structure inside and around a rectangular array of rigid emerged cylinders located at the sidewall of an open channel. *J. Fluid Mech.* **910**, A2.
- KOKEN, M. & CONSTANTINESCU, G. 2023 Influence of submergence ratio on flow and drag forces generated by a long rectangular array of rigid cylinders at the sidewall of an open channel. *J. Fluid Mech.* **966**, A5.
- KRAJNOVIC, S. 2011 Flow around a tall finite cylinder explored by large eddy simulation. *J. Fluid Mech.* **676**, 294–317.
- KUMAR, P. & TIWARI, S. 2019 Effect of incoming shear on unsteady wake in flow past surface mounted polygonal prism. *Phys. Fluids* **31** (11), 113607.
- LECLERCQ, T. & DE LANGRE, E. 2018 Reconfiguration of elastic blades in oscillatory flow. *J. Fluid Mech.* **838**, 606–630.
- LEE, L.W. 1997 Wake structure behind a circular cylinder with a free end. *Proc. Heat Transfer Fluid Mech. Inst.*, 241–251.
- LEONARD, L. & LUTHER, M. 1995 Flow hydrodynamics in tidal marsh canopies. *Limnol. Oceanogr.* **40**, 1474–1484.
- LI, X., WEI, W. & BAI, F. 2020 A full three-dimensional vortex-induced vibration prediction model for top-tensioned risers based on vector form intrinsic finite element method. *Ocean Engng* **218**, 108140.
- LI, Y. & FUHRMAN, D.R. 2022 On the turbulence modelling of waves breaking on a vertical pile. *J. Fluid Mech.* **953**, A3.
- LIU, Y., SO, R.M.C. & CUI, Z.X. 2005 A finite cantilevered cylinder in a cross-flow. *J. Fluids Struct.* **20** (4), 589–609.
- LUHAR, M. 2012 Analytical and experimental studies of plant-flow interaction at multiple scales. *Ph.D. thesis*, Massachusetts Institute of Technology, USA.
- LUHAR, M., COUTU, S., INFANTES, E., FOX, S. & NEPF, H. 2010 Wave induced velocities inside a model seagrass bed. *J. Geophys. Res.* **115** (C12), C12005.
- LUHAR, M. & NEPF, H.M. 2011 Flow-induced reconfiguration of buoyant and flexible aquatic vegetation. *Limnol. Oceanogr.* **56** (6), 2003–2017.
- LUHAR, M. & NEPF, H.M. 2016 Wave-induced dynamics of flexible blades. *J. Fluids Struct.* **61**, 20–41.
- LUO, S.C., GAN, T.L. & CHEW, Y.T. 1996 Uniform flow past one (or two in tandem) finite length circular cylinder(s). *J. Wind Engng Ind. Aerodyn.* **59** (1), 69–93.
- MULLARNEY, J.C. & HENDERSON, S.M. 2010 Wave-forced motion of submerged single-stem vegetation. *J. Geophys. Res.* **115** (C12), C12061.
- MUNSON, B., YOUNG, D. & OKIISHI, T. 1990 *Fundamentals of Fluid Mechanics*. John Wiley.

- NEPF, H.M. 2012 Flow and transport in regions with aquatic vegetation. *Annu. Rev. Fluid Mech.* **44** (1), 123–142.
- NESHAMAR, O.E., VAN DER A, D.A. & O'DONOGHUE, T. 2022 Flow-induced vibration of a cantilevered cylinder in oscillatory flow at high KC. *J. Fluids Struct.* **109**, 103476.
- O'CONNOR, J. & REVELL, A. 2019 Dynamic interactions of multiple wall-mounted flexible flaps. *J. Fluid Mech.* **870**, 189–216.
- PALAU-SALVADOR, G., STOESSER, T., FROHLICH, J., KAPPLER, M. & RODI, W. 2010 Large eddy simulations and experiments of flow around finite-height cylinders. *Flow Turbul. Combust.* **84** (2), 239–275.
- PATTENDEN, R.J., TURNOCK, S.R. & ZHANG, X. 2005 Measurements of the flow over a low-aspect-ratio cylinder mounted on a ground plane. *Exp. Fluids* **39** (1), 10–21.
- PESKIN, C.S. 1972 Flow Patterns Around Heart Valves: a Digital Computer Method for Solving the Equations of Motion school, Yeshiva University.
- PORTEOUS, R., MOREAU, D.J. & DOOLAN, C.J. 2014 A review of flow-induced noise from finite wall-mounted cylinders. *J. Fluids Struct.* **51**, 240–254.
- PY, C., DE LANGRE, E. & MOULIA, B. 2006 A frequency lock-in mechanism in the interaction between wind and crop canopies. *J. Fluid Mech.* **568**, 425–449.
- REVSTEDT, J. 2013 Interaction between an incompressible flow and elastic cantilevers of circular cross-section. *Int J. Heat Fluid Flow* **43**, 244–250.
- ROBINSON, S.K. 1991 Coherent motions in the turbulent boundary layer. *Annu. Rev. Fluid Mech.* **23** (1), 601–639.
- ROTA, G.F., KOSEKI, M., AGRAWAL, R., OLIVIERI, S. & ROSTI, M.E. 2024 Forced and natural dynamics of a clamped flexible fiber in wall turbulence. *Phys. Rev. Fluids* **9** (1), L012601.
- SAEEDI, M., LEPOUDRE, P.P. & WANG, B.C. 2014 Direct numerical simulation of turbulent wake behind a surface-mounted square cylinder. *J. Fluids Struct.* **51**, 20–39.
- SAHA, A.K. 2013 Unsteady flow past a finite square cylinder mounted on a wall at low Reynolds number. *Comput. Fluids* **88**, 599–615.
- SAKAMOTO, H. & ARIE, M. 1983 Vortex shedding from a rectangular prism and a circular cylinder placed vertically in a turbulent boundary layer. *J. Fluid Mech.* **126**, 147–165.
- SARPKAYA, T. 2004 A critical review of the intrinsic nature of vortex-induced vibrations. *J. Fluids Struct.* **19** (4), 389–447.
- SEAL, C.V., SMITH, C.R., AKIN, O. & ROCKWELL, D. 1995 Quantitative characteristics of a laminar, unsteady necklace vortex system at a rectangular block-flat plate juncture. *J. Fluid Mech.* **286**, 117–135.
- SEAL, C.V., SMITH, C.R. & ROCKWELL, D. 1997 Dynamics of the vorticity distribution in Endwall junctions. *AIAA J.* **35** (6), 1041–1047.
- SHIH, C., WANG, Y.K. & TING, E.C. 2004 Fundamentals of a vector form intrinsic finite element: part III, convected material frame and examples. *J. Mech.* **20** (2), 133–143.
- SILVA-LEON, J. & CIONCOLINI, A. 2020 Experiments on flexible filaments in air flow for aeroelasticity and fluid-structure interaction models validation. *Fluids* **5** (2), 90.
- SIMPSON, R.L. 2001 Junction flow. *Annu. Rev. Fluid Mech.* **33** (1), 415–443.
- SMAGORINSKY, J. 1963 General circulation experiments with primitive equations. *Mon. Weath. Rev.* **91** (3), 99–164.
- SUMNER, D. 2013 Flow above the free end of a surface-mounted finite-height circular cylinder: a review. *J. Fluids Struct.* **43**, 41–63.
- SUMNER, D. & HESELTINE, J.L. 2008 Tip vortex structure for a circular cylinder with a free end. *J. Wind Engng Ind. Aerodyn.* **96** (6-7), 1185–1196.
- SUMNER, D., HESELTINE, J.L. & DANSEREAU, O.J.P. 2004 Wake structure of a finite circular cylinder of small aspect ratio. *Exp. Fluids* **37** (5), 720–730.
- TING, E.C., DUAN, Y.F. & WU, D.Y. 2012 *Vector Mechanics of Structures (in Chinese)*. Science Press.
- TING, E.C., SHIH, C. & WANG, Y.-K. 2004a Fundamentals of a vector form intrinsic finite element: part I. Basic procedure and a plane frame element. *J. Mech.* **20** (2), 113–122.
- TING, E.C., SHIH, C. & WANG, Y.-K. 2004b Fundamentals of a vector form intrinsic finite element: part II. plane solid elements. *J. Mech.* **20** (2), 123–132.
- TING, E.C. & WANG, C.Y. 2008 Vector mechanics of solids. Research report, National Central University.
- TRIANTAFYLLOU, M.S., BOURGUET, R., DAHL, J. & MODARRES-SADEGHI, Y. 2016 Vortex induced vibrations. In *Springer Handbook of Ocean Engineering*. Springer International Publishing.
- TSUTSUI, T. 2012 Flow around a cylindrical structure mounted in a plane turbulent boundary layer. *J. Wind Engng Ind. Aerodyn.* **104–106**, 239–247.
- VETTORI, D. & NIKORA, V. 2018 Flow–seaweed interactions: a laboratory study using blade models. *Environ. Fluid Mech.* **18** (3), 611–636.

- WANG, E., XIAO, Q. & INCECIK, A. 2017 Three-dimensional numerical simulation of two-degree-of-freedom VIV of a circular cylinder with varying natural frequency ratios at  $Re = 500$ . *J. Fluids Struct.* **73**, 162–182.
- WANG, H., ZHOU, Y., CHAN, C.K. & LAM, K.S. 2006 Effect of initial conditions on interaction between a boundary layer and a wall-mounted finite-length-cylinder wake. *Phys. Fluids* **18** (6), 065106.
- WANG, H.F., CAO, H.L. & ZHOU, Y. 2014 POD analysis of a finite-length cylinder near wake. *Exp. Fluids* **55**, 1–15.
- WANG, H.F. & ZHOU, Y. 2009 The finite-length square cylinder near wake. *J. Fluid Mech.* **638**, 453–490.
- WEI, Q.D., CHEN, G. & DU, X.D. 2001 An experimental study on the structure of juncture flows. *J. Vis.* **3** (4), 341–348.
- WERNER, H. & WENGLE, H. 1993 Large-eddy simulation of turbulent flow around a cube in a plane channel. In *Selected Papers From the 8th Symposium On Turbulent Shear Flows* (eds. DURST F., FRIEDRICH R., LAUNDER B.E., SCHUMANN U. & WHITELAW J.H.), pp. 155–168, Springer.
- WILLIAMSON, C.H.K. 1996 Three-dimensional wake transition. *J. Fluid Mech.* **328**, 345–407.
- WU, H., ZENG, X., XIAO, J., YU, Y., DAI, X. & YU, J. 2020 Vector form intrinsic finite-element analysis of static and dynamic behavior of deep-sea flexible pipe. *Intl J. Nav. Archit. Ocean Engng* **12**, 376–386.
- XU, L. & LIN, M. 2017 Analysis of buried pipelines subjected to reverse fault motion using the vector form intrinsic finite element method. *Solid Dyn. Earthquake Engng* **93**, 61–83.
- XU, R., LI, D.-X., JIANG, J.-P. & LIU, W. 2015 Nonlinear vibration analysis of membrane SAR antenna structure adopting a vector form intrinsic finite element. *J. Mech.* **31** (3), 269–277.
- YAUWENAS, Y., PORTEOUS, R., MOREAU, D.J. & DOOLAN, C.J. 2019 The effect of aspect ratio on the wake structure of finite wall-mounted square cylinders. *J. Fluid Mech.* **875**, 929–960.
- YU, Z., WANG, E., BAO, Y., XIAO, Q., LI, X., INCECIK, A. & LIN, B. 2024 VIV of two rigidly coupled side-by-side cylinders at subcritical  $Re$ . *Intl J. Mech. Sci.* **267**, 108961.
- ZELLER, R.B., WEITZMAN, J.S., ABBETT, M.E., ZARAMA, F.J., FRINGER, O.B. & KOSEFF, J.R. 2014 Improved parameterization of seagrass blade dynamics and wave attenuation based on numerical and laboratory experiments. *Limnol. Oceanogr.* **59** (1), 251–266.
- ZHANG, D., CHENG, L., AN, H. & DRAPER, S. 2021 Flow around a surface-mounted finite circular cylinder completely submerged within the bottom boundary layer. *Eur. J. Mech. B Fluids* **86**, 169–197.
- ZHANG, D., CHENG, L., AN, H. & ZHAO, M. 2017 Direct numerical simulation of flow around a surface-mounted finite square cylinder at low Reynolds numbers. *Phys. Fluids* **29** (4), 045101.
- ZHANG, X., HE, G. & ZHANG, X. 2020 Fluid–structure interactions of single and dual wall-mounted 2D flexible filaments in a laminar boundary layer. *J. Fluids Struct.* **92**, 102787.
- ZHANG, X. & NEPF, H. 2022 Reconfiguration of and drag on marsh plants in combined waves and current. *J. Fluids Struct.* **110**, 103539.
- ZHU, H.-Y., WANG, C.-Y., WANG, H.-P. & WANG, J.-J. 2017 Tomographic PIV investigation on 3D wake structures for flow over a wall-mounted short cylinder. *J. Fluid Mech.* **831**, 743–778.
- ZHU, L., ZOU, Q., HUGUENARD, K. & FREDRIKSSON, D.W. 2020 Mechanisms for the asymmetric motion of submerged aquatic vegetation in waves: a consistent-mass cable model. *J. Geophys. Res.: Oceans* **125** (2), e2019JC015517.